



Aalborg Universitet

AALBORG UNIVERSITY
DENMARK

Comparative Study of Symmetrical Controlled Grid-Connected Inverters

Gao, Shuning; Zhao, Haoran; Wang, Peng; Gui, Yonghao; Terzija, Vladimir; Blaabjerg, Frede

Published in:
I E E E Transactions on Power Electronics

DOI (link to publication from Publisher):
[10.1109/TPEL.2021.3122002](https://doi.org/10.1109/TPEL.2021.3122002)

Publication date:
2022

Document Version
Accepted author manuscript, peer reviewed version

[Link to publication from Aalborg University](#)

Citation for published version (APA):

Gao, S., Zhao, H., Wang, P., Gui, Y., Terzija, V., & Blaabjerg, F. (2022). Comparative Study of Symmetrical Controlled Grid-Connected Inverters. *I E E E Transactions on Power Electronics*, 37(4), 3954-3968.
<https://doi.org/10.1109/TPEL.2021.3122002>

General rights

Copyright and moral rights for the publications made accessible in the public portal are retained by the authors and/or other copyright owners and it is a condition of accessing publications that users recognise and abide by the legal requirements associated with these rights.

- Users may download and print one copy of any publication from the public portal for the purpose of private study or research.
- You may not further distribute the material or use it for any profit-making activity or commercial gain
- You may freely distribute the URL identifying the publication in the public portal -

Take down policy

If you believe that this document breaches copyright please contact us at vbn@aub.aau.dk providing details, and we will remove access to the work immediately and investigate your claim.

Comparative Study of Symmetrical Controlled Grid-Connected Inverters

Shuning Gao, *Student Member, IEEE*, Haoran Zhao, *Senior Member, IEEE*, Peng Wang, *Member, IEEE*, Yonghao Gui, *Senior Member, IEEE*, Vladimir Terzija, *Fellow, IEEE*, and Frede Blaabjerg, *Fellow, IEEE*

Abstract—The asymmetrical dynamics of the conventional synchronous reference frame phase-locked loop (PLL) enhance the complexity of the system and endanger the stability of the grid-connected voltage source converters. In this paper, the admittance modeling of three different symmetrical control strategies, i.e., voltage oriented control with symmetrical PLL, voltage modulated direct power control, and proportional resonant control, are proposed and uniformed based on the same power tracking property. The voltage feedforward and decoupling of the controllers are both considered. Moreover, due to the symmetrical structure of the three control strategies, their admittance models can directly be modeled under $\alpha\beta$ reference frame as single-input single-output systems. In addition, to reveal the similarity between different control methods and emphasize their differences, the admittance models are constructed by using the same framework. The admittance modeling is verified using frequency-scan, and the control performance is tested using MATLAB/Simulink Simscape Power System and experimental prototype. Finally, the stability criterion based on proposed admittance modeling is verified by simulation results carried out in real-time simulation platform RTLAB from Opal-RT.

Index Terms—Admittance-based analysis, proportional resonant control, voltage oriented control, voltage source converter (VSC), voltage modulated control

I. INTRODUCTION

POWER electronic devices such as voltage source converters (VSCs) have been nowadays widely applied in the modern power system [1]. However, the wideband interactions between the VSC and grid impedance bring potential instability problem to the system and have been brought to the forefront of the academics [2]–[9]. In order to address the challenge, multiple analysis methods have been proposed. Among these methods, the admittance analysis successfully depicts the frequency response of the grid-connected VSC system [10]. Moreover, by equivalenting the system with a Thevenin/Norton equivalent circuit, the admittance based

analysis can easily identify the system stability through the Nyquist stability criterion [4], [6]–[8].

It has been proved that the control strategy of the VSC plays a decisive role in the harmonic interaction between the VSC and power grid [6]. The most typical control strategy of VSC is called voltage oriented control (VOC), which requires a phase-locked loop (PLL) for the grid synchronization [8]. In conventional synchronous reference frame PLL (SRF-PLL), the phase signal of the grid voltage is extracted only by its q-axis component. Therefore, it is inherently asymmetric, which brings a frequency-coupling phenomenon and greatly enhances the complexity of the admittance model [7], [8]. Usually, due to the inherent asymmetrical characteristic, the admittance of the inverter using VOC has to be modeled in the form of a matrix as a multi-input multi-output (MIMO) system [11]. The impedance matrix can be established in the dq reference frame for simplicity. The stability analysis based on dq frame model requires using generalized Nyquist stability criterion [6]. Moreover, the analysis based on dq frame model is not easy to interpret the mechanism of frequency-coupling [12]. The $\alpha\beta$ admittance modeling method based on harmonic linearization is proposed [12], [13]. The $\alpha\beta$ frame admittance modeling approach can readily describe the system in the same coordinate system, thus has a more intuitive physical meaning [14], [15]. The neglecting of cross-coupled components in the $\alpha\beta$ modeling leads to inaccuracy of the stability analysis [7]. To describe the generation of coupled components, a complex equivalence method is proposed in [7], which also unifies the dq frame and $\alpha\beta$ frame admittance modeling methods. The coupling is regarded as a conjugate of the corresponding vector under the dq reference frame.

A symmetrical PLL (S-PLL) is proposed in [8]. Compared to SRF-PLL, the S-PLL also tracks the voltage magnitude using a defined imaginary part of the voltage phase signal, thereby it exhibits symmetrical characteristics and eliminates the generation of frequency-coupling components. The S-PLL based VOC (S-VOC) can also be applied into the doubly-fed induction generator for impedance characteristics reshaping and improvement of grid-integration stability [16].

The proportional-resonant (PR) control is also a typical control strategy designed for grid-connected inverters [17]–[21]. Using PR control can reduce the system complexity since it avoids PLL for grid synchronization [21]. It is constructed directly under the $\alpha\beta$ reference frame with a symmetrical structure and can realize zero ac tracking error. However, the control performance cannot be guaranteed once the grid voltage frequency is deviated [18]. A stability assessment of

This work was supported by National Key R&D Program of China under grant 2018YFA0702200.

S. Gao is with the School of Electrical Engineering, Shandong University, Jinan 250061, China, and was also with the Automation & Control Section at the Department of Electronic Systems, Aalborg University, 9220 Aalborg, Denmark (email:gaosn@mail.sdu.edu.cn).

H. Zhao and P. Wang are with the School of Electrical Engineering, Shandong University, Ji'nan 250061, China (email:hzhao@sdu.edu.cn, wang-pengtu@gmail.com).

Y. Gui is with Automation & Control Section, Department of Electronic Systems, Aalborg University, 9220 Aalborg, Denmark (e-mail:yg@es.aau.dk).

V. Terzija is with the Skolkovo Institute of Science and Technology, Bolshoy Boulevard 30, bld. 1, Moscow, Russia 121205 (email: v.terzija@skoltech.ru).

F. Blaabjerg is with Department of Energy Technology, Aalborg University, 9220 Aalborg, Denmark (e-mail:fbl@et.aau.dk).

the grid-connected VSC using PR is proposed in [22]. The paper focuses on the direct-voltage control, and the power control is not included.

Direct power control (DPC) is also a widely-studied VSC control strategy, which successfully avoids the use of PLL [23]–[27]. Conventional look-up-table (LUT) based DPC has an nonfixed switching frequency, which deteriorates its steady-state control performance. In recent decades, improved DPC methods such as voltage modulated (VM)-DPC and sliding-mode control (SMC) [24] are proposed and widely applied [25]. They obtain constant switching frequency by using space vector modulation (SVM) techniques and thus have better steady-state performance compared to the conventional DPC methods. The VM-DPC is recently proved to be effective and widely applicable [26], [28], [29]. It improves the performance of VSC compared with SMC and LUT-DPC. In addition, the VM-DPC maintains a satisfactory steady-state performance similar to that of conventional VOC [25]. The VM-DPC is a symmetrical control method, and its admittance model can be linearized and built directly under $\alpha\beta$ frame [30]. Note the VM-DPC still brings frequency coupling phenomenon due to the inherent power integration. However, the coupling can be restrained by using a band-pass filter.

Note that it is normally difficult to compare the admittance characteristics of different control methods fairly. Partly because the control parameters are always selected based on a specific control structure to meet the best performance, i.e., the best input reference tracking property. Therefore, one of the purposes of this paper is to unify the power tracking properties of three different symmetrical controllers, i.e., S-VOC, PR control, and VM-DPC. Among three control methods, S-VOC and PR are both typical linear control methods, and the VM-DPC is a DPC method using SVM. Then, based on the same power tracking property, the admittance characteristics of the three control strategies are presented and compared in detail. The innovations can be summarized as follows,

- 1) The power tracking properties of three different symmetrical control methods are described by using a unified second-order transfer function. The unified control performance of three controllers is verified using simulation carried out in MATLAB/Simulink Simscape Electrical and experimental prototype.
- 2) The admittance models of three symmetrical controllers are summarized. To further reveal interconnection and the difference between the three control methods, the proposed admittances are presented as a unified basic admittance plus additional virtual admittance determined by different controllers. The admittances are modeled directly under the $\alpha\beta$ reference frame with a clear physical meaning.
- 3) The effects of the three symmetrical control structures on the harmonic response and stability of grid-connected inverters are compared. The accuracy of the Nyquist stability analysis based on the proposed admittance modelling method is verified using real-time simulation platform RTLAB from Opal-RT.

The rest of the paper is organized as follows: an overview

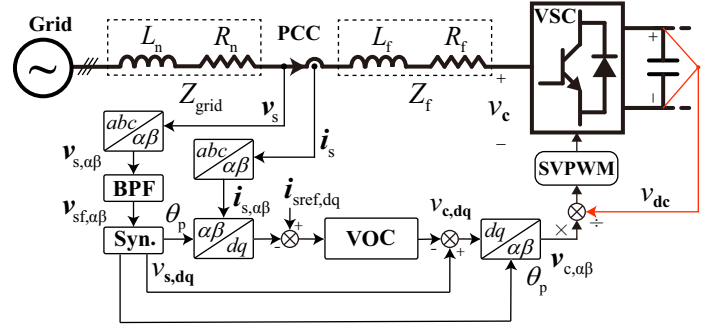


Fig. 1. Diagram of grid-connected voltage source converter (VSC) using voltage oriented control (VOC).

of the admittance analysis of VSC using conventional VOC and frequency-coupling phenomenon caused by SRF-PLL are discussed in Section II. The admittance modeling of three different symmetrical control strategies is presented in Section III. A unified performance analysis is presented in Section IV. In Section V, the admittance modeling methods of three symmetrical controllers are presented. Section VI presents the simulation results and finally, the conclusions are given in Section VI.

II. OVERVIEW OF ADMITTANCE ANALYSIS OF VOC BASED GRID-CONNECTED INVERTERS

To better introduce the concept of symmetrical control, an overview of the admittance analysis of the conventional VOC is introduced. Moreover, the frequency-coupling phenomenon caused by SRF-PLL is explained using the $\alpha\beta$ frame admittance model. This study focuses on the inner-loop dynamics, and the dc voltage is considered to be constant. Moreover, the dynamics of PWM is neglected in the admittance modeling. The modulation is considered to be capable of generating output as an ideal voltage waveform.

A. Voltage Oriented Control of VSC

A typical grid-connected VSC is presented in Fig.1, where the complex space vectors of the voltage and current can be denoted by the sum of their fundamental components and harmonic components using boldface letters, e.g., $\mathbf{v}_s = \mathbf{v}_{s1} + \tilde{\mathbf{v}}_{sh}$, $\mathbf{i}_s = \mathbf{i}_{s1} + \tilde{\mathbf{i}}_{sh}$. Take the point of common coupling (PCC) voltage \mathbf{v}_s as an example, the space vector can either be presented under $\alpha\beta$ or under dq frame as,

$$\begin{aligned} \mathbf{v}_s &= \underbrace{v_{s1,\alpha} + jv_{s1,\beta}}_{\mathbf{v}_{s1,\alpha\beta}} + \underbrace{\tilde{v}_{sh,\alpha} + j\tilde{v}_{sh,\beta}}_{\tilde{\mathbf{v}}_{sh,\alpha\beta}} \\ \mathbf{v}_s &= \underbrace{v_{s1,d} + jv_{s1,q}}_{\mathbf{v}_{s1,dq}} + \underbrace{\tilde{v}_{sh,d} + j\tilde{v}_{sh,q}}_{\tilde{\mathbf{v}}_{sh,dq}} \end{aligned} \quad (1)$$

The basic equation of the grid-connected VSC is,

$$\mathbf{v}_s - \mathbf{v}_c = R_f \mathbf{i}_s + L_f \frac{d\mathbf{i}_s}{dt} \quad (2)$$

where \mathbf{v}_c and \mathbf{i}_s are the VSC voltage and output current, R_f and L_f are the resistance and inductance of VSC filter. Using

(2), the fundamental components of the grid-connected VSC can be also written in s' domain under dq frame as,

$$\mathbf{v}_{s1,dq} - \mathbf{v}_{c1,dq} = [R_f + (s' + j\omega_s)L_f]\mathbf{i}_{s1,dq} \quad (3)$$

where $\mathbf{v}_{c1,dq}$, $\mathbf{i}_{s1,dq}$ are the fundamental space vectors of the VSC voltage and the current under dq frame, respectively. ω_s denotes the fundamental frequency of the grid voltage. The relation can be translated into the stationary reference frame using $s = s' + j\omega_s$, and the equation of the harmonic components can be expressed in $\alpha\beta$ frame as,

$$\tilde{\mathbf{v}}_{sh,\alpha\beta} - \tilde{\mathbf{v}}_{ch,\alpha\beta} = (R_f + sL_f)\tilde{\mathbf{i}}_{sh,\alpha\beta}, \quad (4)$$

where $\tilde{\mathbf{v}}_{ch,\alpha\beta}$, $\tilde{\mathbf{i}}_{sh,\alpha\beta}$ denote the harmonic components of $\mathbf{v}_{c,\alpha\beta}$, and $\mathbf{i}_{s,\alpha\beta}$, respectively. The filter admittance is denoted by $Y_f = 1/Z_f(s) = 1/(R_f + sL_f)$.

The voltage harmonics \mathbf{v}_{sh} at the PCC may deteriorate the performance of the PLL and VSC controller. Therefore, a band-pass filter (BPF) is utilized in this paper to block the harmonics and dc components in the measured PCC voltage. The transfer function of the BPF can be expressed in the $\alpha\beta$ frame as follows:

$$G_{fil}(s) = \frac{2\omega_c s}{s^2 + 2\omega_c s + \omega_s^2}, \quad (5)$$

where $\omega_c = \zeta_f \omega_s$ is the resonance bandwidth of the BPF, and ζ_f is the damping ratio of the BPF. Note that $G_{fil}(j\omega_s) = 1$. Therefore, the voltage input of the controller can be expressed under $\alpha\beta$ and dq reference frames, respectively, as follows,

$$\begin{aligned} \mathbf{v}_{sf,\alpha\beta} &= \mathbf{v}_{s1,\alpha\beta} + \underbrace{G_{fil}(s)\tilde{\mathbf{v}}_{sh,\alpha\beta}}_{\tilde{\mathbf{v}}_{shf,\alpha\beta}} \\ \mathbf{v}_{sf,dq} &= \mathbf{v}_{s1,dq} + \underbrace{G_{fil}(s' + j\omega_s)\tilde{\mathbf{v}}_{sh,dq}}_{\tilde{\mathbf{v}}_{shf,dq}}, \end{aligned} \quad (6)$$

where $\tilde{\mathbf{v}}_{shf,\alpha\beta}$ and $\tilde{\mathbf{v}}_{shf,dq}$ denote the filtered voltage input under $\alpha\beta$ and dq reference frames, respectively. Note that the most typical control used in practical VSC is the symmetrically decoupled PI control consisting of current feedforward decoupling and voltage feedforward linearization components. Therefore, the fundamental component of the VSC voltage $\mathbf{v}_{c1,dq}$ can be expressed in terms of the fundamental components in the dq reference frame as,

$$\mathbf{v}_{c1,dq} = -L_f \underbrace{\left(K_p + \frac{K_i}{s'}\right)}_{G_{PI,dq}(s')} (\mathbf{i}_{sref,dq} - \mathbf{i}_{s1,dq}) - \underbrace{j\omega_s L_f \mathbf{i}_{s1,dq} + \mathbf{v}_{s1,dq}}_{\text{current/voltage feedforward}}, \quad (7)$$

where $G_{PI,dq}(s')$ denotes the basic PI control unit, K_p and K_i are the PI control parameters. The current references $\mathbf{i}_{sref,dq}$ and the current fundamental component $\mathbf{i}_{s1,dq}$ can be calculated as follows,

$$\mathbf{i}_{sref,dq} = -\frac{2}{3} \frac{S_{sref}}{|v_{s1}|} \mathbf{i}_{s1,dq} = -\frac{2}{3} \frac{S_{s1}}{|v_{s1}|}, \quad (8)$$

where $S_{sref} = P_{sref} + jQ_{sref}$ denotes the reference of output complex power. $S_{s1} = P_{s1} + jQ_{s1} = -\frac{3}{2}[\text{Re}(\mathbf{v}_{s1} \mathbf{i}_{s1}^*) + j\text{Im}(\mathbf{v}_{s1} \mathbf{i}_{s1}^*)]$ represents the fundamental components of the

instantaneous complex power. By neglecting the harmonic components and the dynamics of time delay, the power tracking dynamics can be described as a second-order transfer function by substituting (6), (7) into (3),

$$T_{VSC}^{PI} = \frac{\mathbf{i}_{s1,dq}}{\mathbf{i}_{sref,dq}} = \frac{S_{s1,dq}}{S_{sref,dq}} = \frac{K_p s' + K_i}{s'^2 + (K_p + \frac{R_f}{L_f})s' + K_i}. \quad (9)$$

To ensure the performance of fundamental dc regulation, normally, the control parameters can be chosen based on the natural frequency ω_n and damping factor ζ derived from the characteristic polynomial of (9) [31],

$$\begin{cases} K_i = \omega_n^2 \\ K_p = 2\zeta_n \omega_n - \frac{R_f}{L_f} \end{cases}. \quad (10)$$

Except for the fundamental components, the voltage output is also affected by the current and voltage harmonics as follows,

$$\tilde{\mathbf{v}}_{ch,dq} = G_{del}(s) \underbrace{[(L_f G_{PI,dq}(s') - j\omega_s L_f)\tilde{\mathbf{i}}_{sh,dq} + \tilde{\mathbf{v}}_{shf,dq}]}_{G_{c,dq}(s')}, \quad (11)$$

where $G_{c,dq}(s')$ denotes the influence of PI control with feedforward on VSC voltage harmonics. Note that the time delay dynamics represented by $G_{del}(s)$ is [7], [22],

$$G_{del}(s) = e^{-1.5T_{del}s} \approx \frac{1 - 1.5T_{del}s}{1 + 1.5T_{del}s} \quad (12)$$

where T_{del} is the sampling period. Using the frequency translation $s' = s - j\omega_s$, $\tilde{\mathbf{v}}_{ch,dq}$ can also be written under the $\alpha\beta$ frame as,

$$\begin{aligned} \tilde{\mathbf{v}}_{ch,\alpha\beta} &= G_{del}(s) \underbrace{[(L_f G_{PI,\alpha\beta}(s - j\omega_s) - j\omega_s L_f)\tilde{\mathbf{i}}_{sh,\alpha\beta}]}_{G_{c,\alpha\beta}(s - j\omega_s)} \\ &\quad + \tilde{\mathbf{v}}_{shf,\alpha\beta}, \end{aligned} \quad (13)$$

The admittance of VSC with the PI control, denoting its harmonic-domain response, can be derived in the $\alpha\beta$ reference frame by substituting (6) and (13) into (4) as follows,

$$Y_{VSC}^{PI} = \frac{\tilde{\mathbf{i}}_{sh,\alpha\beta}}{\tilde{\mathbf{v}}_{sh,\alpha\beta}} = \frac{Y_f(s)[1 - G_{del}(s)G_{fil}(s)]}{1 + G_{del}(s)Y_f(s)G_{c,\alpha\beta}(s - j\omega_s)}. \quad (14)$$

Note that T_{VSC}^{PI} and Y_{VSC}^{PI} represents the power tracking property and the response to the voltage harmonics, respectively. Y_{VSC}^{PI} mainly affects the small-signal stability of the grid-connected VSC under weak-grid conditions. Moreover, it can be found that Y_{VSC}^{PI} is only related to the control parameters and has no relation with the system operation point.

B. SRF-PLL and Frequency Coupling Phenomenon

Recent studies revealed that the SRF-PLL affects the harmonic response of the system and introduced frequency coupling phenomenon due to its asymmetrical structure. For the modeling of SRF-PLL, an $\alpha\beta$ frame admittance modeling presented in [7] is used in this section. The input of the PLL is a filtered PCC voltage $\mathbf{v}_{sf,\alpha\beta}^s$ under the $\alpha\beta$ reference frame, the dq-transformation using SRF-PLL can be decomposed as follows,

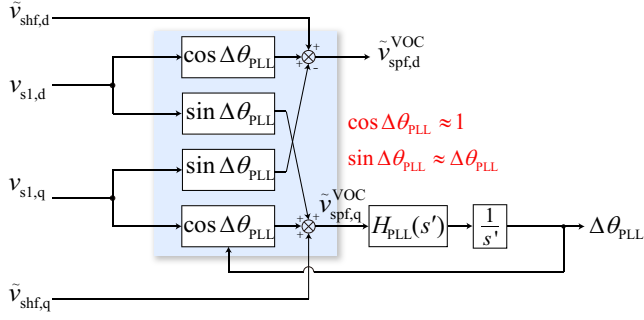


Fig. 2. Small-signal block diagram of the conventional single-reference frame phase-locked-loop (SRF-PLL).

$$\begin{aligned}
 v_{sf,dq}^c &= v_{sf,\alpha\beta}^s e^{-j\theta_p} \\
 &= v_{sf,dq}^s e^{-j\Delta\theta_{PLL}} = (v_{s1,dq}^s + \tilde{v}_{shf,dq}^s) e^{-j\Delta\theta_{PLL}} \\
 &\approx (v_{s1,dq}^s + \tilde{v}_{shf,dq}^s)(1 - j\Delta\theta_{PLL}) \\
 &= v_{s1,dq}^s + \underbrace{\tilde{v}_{shf,dq}^s - jv_{s1,dq}^s \Delta\theta_{PLL}}_{\tilde{v}_{spf,dq}^{VOC}} - \underbrace{j\tilde{v}_{shf,dq}^s \Delta\theta_{PLL}}_{\text{Negligible}}
 \end{aligned} \quad (15)$$

where the superscripts '*s*' and '*c*' denote the grid *dq* reference frame and PLL *dq* reference frame, respectively. $\theta_p = \omega_s t + \Delta\theta_{PLL}$ is the detected voltage phase angle. Note that $v_{s1,dq}^s$ represents the fundamental components of the voltage, under *dq* reference frame, $v_{s1,dq}^s = |v_{s1}|$. The effect of the PLL tracking error to the harmonic components is very small thus it can be neglected, i.e., $\tilde{v}_{shf,dq}^s \approx \tilde{v}_{shf,dq}^c$. Therefore, the superscripts '*c*' and '*s*' are ignored in the following. $\Delta\theta_{PLL}$ is the error between the detected voltage phase and actual grid voltage phase value. $\tilde{v}_{shf,dq}^s \Delta\theta_{PLL}$ denotes the coupling between voltage harmonics and the error of phase measurement, which is small enough to be neglected. The total variation of the measured voltage can be defined as $\tilde{v}_{spf,dq}^{VOC}$. Note that $\tilde{v}_{spf,dq}^{VOC}$ can be separately presented by its *d* and *q* axis components as follows,

$$\begin{cases} \tilde{v}_{spf,d}^{VOC} = \tilde{v}_{shf,d} \\ \tilde{v}_{spf,q}^{VOC} = \tilde{v}_{shf,q} - |v_{s1}| \Delta\theta_{PLL} \end{cases} \quad (16)$$

The SRF-PLL is designed based on the variation of the *q*-axis voltage component $\tilde{v}_{spf,q}^{VOC}$,

$$\Delta\theta_{PLL} = \frac{1}{s'} \underbrace{(K_{PLL,p} + \frac{K_{PLL,i}}{s'})}_{H_{PLL}(s')} \tilde{v}_{spf,q}^{VOC} \quad (17)$$

where $K_{PLL,p}$ and $K_{PLL,i}$ denote the parameters of SRF-PLL. By substituting (17) into (16), the following is obtained,

$$\Delta\theta_{PLL} = \frac{H_{PLL}(s')}{s' + |v_{s1}| H_{PLL}(s')} \tilde{v}_{shf,q} \quad (18)$$

The small-signal block diagram of the conventional SRF-PLL is shown in Fig. 2. Note that the main reason of the frequency-coupling caused by SRF-PLL is its inherent unsymmetrical structure. The one-dimensional voltage input

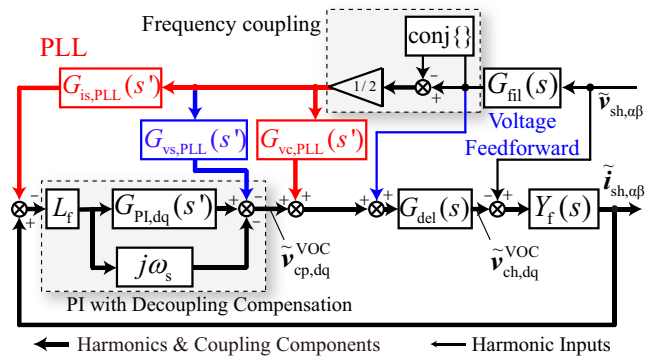


Fig. 3. Small-signal block diagram of grid-connected voltage source converter using SRF-PLL based VOC.

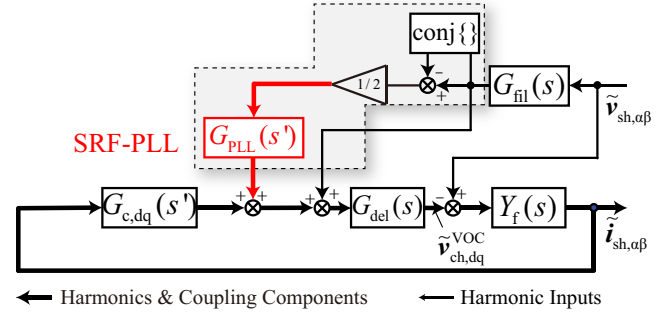


Fig. 4. Simplified small-signal block diagram of grid-connected voltage source converter using SRF-PLL based VOC.

under *q* axis $v_{shf,q}$ can be seen as the sum of two conjugated vectors, i.e., $\tilde{v}_{shf,dq}$ and $\tilde{v}_{shf,dq}^*$ [7], [8]. Therefore, the phase variation $\Delta\theta_{PLL}$ can be expressed as,

$$\Delta\theta_{PLL} = T_{PLL}(s') \frac{\tilde{v}_{shf,dq} - \tilde{v}_{shf,dq}^*}{2j} \quad (19)$$

Based on the derivation similar to (15), the current harmonic components of the control signal is depicted as follows,

$$\tilde{i}_{sp,dq}^{VOC} = \tilde{i}_{sh,dq} - j\tilde{i}_{s1,dq} \Delta\theta_{PLL} \quad (20)$$

The controlled VSC voltage is also affected by the PLL during the inversion *dq* transform, which can be derived as

$$\tilde{v}_{ch,dq}^{VOC} = \tilde{v}_{cp,dq} + jv_{c1,dq} \Delta\theta_{PLL} \quad (21)$$

Therefore, the harmonics of the components can be derived by substituting (19) into (15), (20) and (21) given as,

$$\begin{aligned}
 \tilde{v}_{spf,dq}^{VOC} &= \tilde{v}_{shf,dq} - \underbrace{T_{PLL}(s') v_{s1,dq}}_{G_{vs,pil}(s')} \frac{\tilde{v}_{shf,dq} - \tilde{v}_{shf,dq}^*}{2} \\
 \tilde{i}_{sp,dq}^{VOC} &= \tilde{i}_{sh,dq} - \underbrace{T_{PLL}(s') i_{s1,dq}}_{G_{is,pil}(s')} \frac{\tilde{v}_{shf,dq} - \tilde{v}_{shf,dq}^*}{2} \\
 \tilde{v}_{ch,dq}^{VOC} &= G_{del}(s) [\tilde{v}_{cp,dq}^{VOC} + \underbrace{T_{PLL}(s') v_{c1,dq}}_{G_{vc,pil}(s')} \frac{\tilde{v}_{shf,dq} - \tilde{v}_{shf,dq}^*}{2}]
 \end{aligned} \quad (22)$$

where $G_{is,pil}(s')$ denotes the effect of asymmetrical SRF-PLL on the current inputs. $G_{vc,pil}(s')$ represents the influence of

the SRF-PLL on the dq inverse transformation of the VSC output voltage and $G_{vs,pll}(s')$ express the effect of the SRF-PLL on voltage feedforward components. For simplicity, the harmonics of the VSC voltage is considered to be equal to the output signal $v_{ch,dq}^{PLL}$. Therefore, the effect of VOC and PLL on the control can be expressed as,

$$\tilde{v}_{ch,dq}^{VOC} = G_{del}(s)[G_{c,dq}(s')\tilde{i}_{sp,dq}^{VOC} + \tilde{v}_{spf,dq}^{VOC} + G_{vc,pll}(s')\frac{\tilde{v}_{shf,dq} - \tilde{v}_{shf,dq}^*}{2}]. \quad (23)$$

The small-signal block diagram of the conventional VOC is shown in Fig. 3. Furthermore, (23) can be simplified as follows,

$$\tilde{v}_{ch,dq}^{VOC} = \tilde{v}_{ch1,dq}^{VOC} + \tilde{v}_{ch2,dq}^{VOC} \quad (24)$$

where $\tilde{v}_{ch1,dq}^{VOC}$ and $\tilde{v}_{ch2,dq}^{VOC}$ denote the positive-sequence components and coupling components of the controlled VSC voltage, separately,

$$\begin{cases} \tilde{v}_{ch1,dq}^{VOC} = G_{del}(s)(G_{c,dq}(s')\tilde{i}_{sh,dq} + \tilde{v}_{shf,dq} + \frac{1}{2}G_{PLL}(s')\tilde{v}_{shf,dq}) \\ \tilde{v}_{ch2,dq}^{VOC} = \frac{1}{2}G_{del}(s)G_{PLL}(s')\tilde{v}_{shf,dq}^* \end{cases} \quad (25)$$

where $G_{PLL}(s')$ denotes the effect of PLL on the system harmonic response,

$$G_{PLL}(s') = -G_{c,dq}(s')G_{is,pll}(s') - G_{vs,pll}(s') + G_{vc,pll}(s'). \quad (26)$$

Using (24), the small-signal block diagram of VOC can be simplified as shown in Fig. 4. Due to the frequency-coupling effect caused by the SRF-PLL, the harmonics disturbance v_{sh} at PCC generates two components with different frequencies, i.e., $\tilde{v}_{ch1,dq}^{VOC}$ at $\omega_s - \omega_h$ and $\tilde{v}_{ch2,dq}^{VOC}$ at $\omega_h - \omega_s$, in the VSC output voltage. The generation process of the current coupling-component $\tilde{i}_{sh2,dq}$ under dq reference frame, i.e., the coupling components under $\alpha\beta$ reference frame $\tilde{i}_{sh2,\alpha\beta}$ with frequency $2\omega_s - \omega_h$ can be summarized as follows,

$$\tilde{v}_{sh,\alpha\beta} \rightarrow \tilde{v}_{sh,dq} \begin{cases} \tilde{v}_{ch1,dq}^{VOC}|_{\omega_h - \omega_s} \rightarrow \tilde{i}_{sh1,\alpha\beta}|_{\omega_h} \\ \tilde{v}_{ch2,dq}^{VOC}|_{\omega_s - \omega_h} \rightarrow \tilde{i}_{sh2,\alpha\beta}|_{2\omega_s - \omega_h} \end{cases} \quad (27)$$

III. SYMMETRICAL CONTROL

In this section, the three different symmetrical control methods, i.e., S-VOC, VM-DPC, and PR, are introduced and compared.

A. VOC Using Symmetrical PLL (S-VOC)

The unsymmetrical PLL can be transformed into a symmetrical one by replacing the original phase angle with a complex one $\theta = \theta_d + j\theta_q$ [8]. Using the complex phase angle and the approximation similar to (15), the dq-transformation carried out by the symmetrical PLL can be expressed as,

$$\begin{aligned} v_{s,dq} &= (|v_{s1}| + \tilde{v}_{shf,dq})e^{-j\Delta\theta_{PLL}} \\ &\approx (|v_{s1}| + \underbrace{\tilde{v}_{shf,dq} - |v_{s1}|\Delta\theta_{PLL}}_{\tilde{v}_{spf,dq}^{SVOC}}), \end{aligned} \quad (28)$$

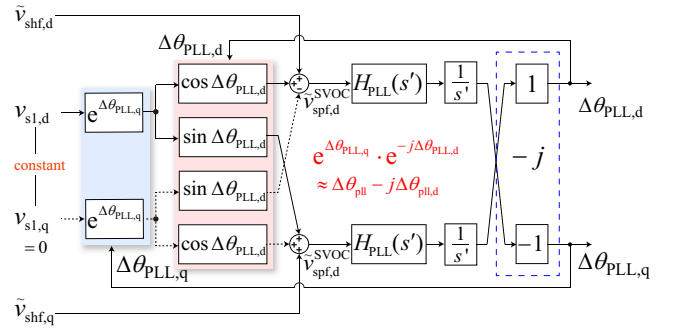


Fig. 5. Small-signal block diagram of the symmetrical phase-locked loop (PLL).

where the phase and magnitude oscillation caused by the voltage harmonics can be approximated as $e^{-j\Delta\theta_{PLL}} \approx \Delta\theta_{PLL,q} - j\Delta\theta_{PLL,d}$. $\Delta\theta_{PLL,d}$ represents the phase tracking error. The additional $\Delta\theta_{PLL,q}$ denotes the voltage magnitude oscillation caused by the harmonics. Therefore, the disturbance of the measured voltage signal $\tilde{v}_{spf,dq}^{SVOC}$ in the symmetrical PLL can be expressed as,

$$\begin{cases} \tilde{v}_{spf,d}^{SVOC} = \tilde{v}_{shf,d} - |v_{s1}|\Delta\theta_{PLL,q} \\ \tilde{v}_{spf,q}^{SVOC} = \tilde{v}_{shf,q} - |v_{s1}|\Delta\theta_{PLL,d} \end{cases} \quad (29)$$

Compared to (16), it shows that error of the voltage magnitude $\tilde{v}_{spf,d}^{SVOC}$ is also tracked by $\Delta\theta_{PLL,q}$. The structure is overall a symmetrical one. Therefore, using the definition of $\Delta\theta_{PLL}$, the symmetrical PLL is designed as,

$$\Delta\theta_{PLL} = -j\frac{1}{s'}H_{PLL}(s')\tilde{v}_{spf,dq}^{SVOC} \quad (30)$$

The equivalent small-signal model of the symmetrical PLL is shown in Fig. 5. Substituting (30) into (29) yields,

$$\Delta\theta_{PLL} = -jT_{PLL}(s')\tilde{v}_{shf,dq}. \quad (31)$$

Compared to (19), the conjugate part $\tilde{v}_{shf,dq}^*$ is eliminated. Therefore, the output VSC voltage signal can be simplified as,

$$\tilde{v}_{ch,dq}^{VOC} = G_{del}(s)G_{c,dq}(s')\tilde{i}_{sh,dq} + G_{del}(s)G_{fil}(s)[1 + G_{PLL}(s')]\tilde{v}_{sh,dq}. \quad (32)$$

Similar to (13), the expression of (32) in the $\alpha\beta$ frame can be found by replacing s' with $s - j\omega_s$ given as,

$$\tilde{v}_{ch,\alpha\beta}^{VOC} = G_{del}(s)G_{c,\alpha\beta}(s - j\omega_s)\tilde{i}_{sh,\alpha\beta} + G_{del}(s)G_{fil}(s)[1 + G_{PLL}(s - j\omega_s)]\tilde{v}_{sh,\alpha\beta}. \quad (33)$$

Since the the harmonic admittance of VSC using symmetrical PLL can be expressed as a SISO system, based on the basic admittance Y_{VSC}^{PI} , the equivalent admittance of the grid-connected VSC using symmetrical PLL based VOC can be deduced by substituting (32) into (3) as follows,

$$Y_{VSC}^{SVOC} = \frac{\tilde{i}_{sh,\alpha\beta}}{\tilde{v}_{sh,\alpha\beta}} = Y_{VSC}^{PI} + Y_n^{SVOC}, \quad (34)$$

where Y_n^{SVOC} denotes the additional virtual admittance of the symmetrical PLL on the original Y_{VSC}^{PI} . The expression of Y_n^{SVOC} is,

$$Y_n^{SVOC} = [1 + Y_f(s)G_{c,\alpha\beta}(s - j\omega_s)]^{-1} Y_f(s) \cdot G_{fil}(s)G_{PLL}(s - j\omega_s). \quad (35)$$

Note that the value of the voltage magnitude $|v_{s1}|$ in symmetrical PLL should be updated in real-time according to the system operation point.

B. Proportional Resonant Control

The basic control structure of a PR control is shown in Fig. 6. The outer loop can be written in terms of complex vectors as,

$$\mathbf{i}_{sref,\alpha\beta} = -\frac{2}{3} \frac{1}{|\mathbf{v}_{sf}^2|} \mathbf{v}_{sf,\alpha\beta} (P_{sref} - jQ_{sref}). \quad (36)$$

The PR current controller using ideal decoupled proportional and reduced-order generalized integrator (ROGI) has following transfer function ,

$$\begin{aligned} \mathbf{v}_{c,\alpha\beta}^{PR} &= \mathbf{v}_{c1,\alpha\beta}^{PR} + \tilde{\mathbf{v}}_{ch,\alpha\beta}^{PR} \\ &= -L_f \left(K_p + \frac{K_i}{s - j\omega_s} \right) (\mathbf{i}_{sref,\alpha\beta} - \mathbf{i}_{s,\alpha\beta}) \\ &\quad - j\omega_s L_f \mathbf{i}_{s,\alpha\beta} + \mathbf{v}_{sf,\alpha\beta} \end{aligned} \quad (37)$$

For the sake of reducing the computation burden, the ROGI is often merged into a second-order generalized integrator (SOGI) as $K_p + K_i/(s - j\omega_s) \rightarrow K_p + 2K_i s / (s^2 + \omega_s^2)$ [22]. Since the main control of PR using SOGI is different from $G_{c,\alpha\beta}(s)$. Therefore, to maintain unity, only PR control with ROGI is considered in this paper. The control block diagram of the PR control is presented in Fig. 6. The fundamental components in (37) can be re-configured and expressed in dq reference frame as follows,

$$\begin{aligned} \mathbf{v}_{c1,dq} &= -L_f \left(K_p + \frac{K_i}{s'} \right) (\mathbf{i}_{sref,dq} - \mathbf{i}_{s1,dq}) \\ &\quad - j\omega_s L_f \mathbf{i}_{s1,dq} + \mathbf{v}_{s1,dq} \end{aligned} \quad (38)$$

By substituting (38) into (3), the transient dynamics of the fundamental current component tracking can be derived as the same as (9). Therefore, it can be concluded that the S-VOC and PR share the same power tracking property. By dividing the current input into $\mathbf{i}_{s,\alpha\beta} = \mathbf{i}_{s1,\alpha\beta} + \tilde{\mathbf{i}}_{sh,\alpha\beta}$ the harmonic components of the VSC output voltage can be deduced by substituting (36) into (37) as,

$$\begin{aligned} \tilde{\mathbf{v}}_{ch,\alpha\beta} &= G_{del}(s)G_{c,\alpha\beta}(s)\tilde{\mathbf{i}}_{sh,\alpha\beta} + \\ &\quad G_{del}(s)G_{fil}(s)[1 + G_{PR}(s)]\tilde{\mathbf{v}}_{sh,\alpha\beta}, \end{aligned} \quad (39)$$

where $G_{PR}(s)$ can be expressed as,

$$G_{PR}(s) = \frac{2L_f}{3|\mathbf{v}_{s1}^2|} \left(K_p + \frac{2K_i s}{s^2 + \omega_s^2} \right) (P_{sref} - jQ_{sref}). \quad (40)$$

The coupling in $|\mathbf{v}_{sf}^2|$ is not considered in the admittance model, i.e., $|\mathbf{v}_{sf}^2|$ is simplified as a known constant $|\mathbf{v}_{s1}^2|$ in (40). Note that a constant value $|\mathbf{v}_{s1}^2|$ can be used to replace the real-time calculation of $|\mathbf{v}_{sf}^2|$ in (36) for the sake of eliminating the

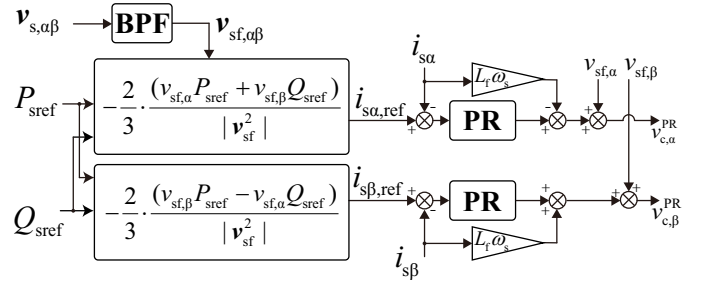


Fig. 6. Block diagram of proportional resonant (PR) control.

coupling terms. However, it sacrifices the accuracy of power tracking once the system operation point changes.

The harmonic admittance of the VSC using PR control can be derived by substituting (39) into (4) as follows,

$$\mathbf{Y}_{VSC}^{PR} = \frac{\tilde{\mathbf{i}}_{sh,\alpha\beta}}{\tilde{\mathbf{v}}_{sh,\alpha\beta}} = Y_{VSC}^{PI} + Y_n^{PR}, \quad (41)$$

where Y_n^{PR} denotes the influence of PR control on VSC system admittance,

$$\mathbf{Y}_n^{PR} = -[1 + G_{del}(s)Y_f(s)G_{c,\alpha\beta}(s - j\omega_s)]^{-1} \cdot Y_f(s)G_{del}(s)G_{fil}(s)G_{PR}(s). \quad (42)$$

C. VM-DPC Control

VM-DPC is a symmetrical control strategy designed directly in $\alpha\beta$ reference frame. The method guarantees power tracking without using PLL with zero steady-state error. A brief introduction of the control scheme is presented firstly in this subsection. The instantaneous powers of the VSC can be expressed as,

$$\begin{cases} P_{sf} = P_{s1} + P_{shf} = -\frac{3}{2} \text{Re}(\mathbf{v}_{sf} \mathbf{i}_s^*) \\ Q_{sf} = Q_{s1} + Q_{shf} = -\frac{3}{2} \text{Im}(\mathbf{v}_{sf} \mathbf{i}_s^*) \end{cases}, \quad (43)$$

where P_{shf} and Q_{shf} denote the instantaneous powers generated by the harmonics of PCC voltage and output current. \mathbf{i}_s^* is the conjugate of \mathbf{i}_s . The differential of powers are presented as,

$$\begin{cases} \frac{dP_{sf}}{dt} = -\frac{3}{2} \text{Re} \left(\frac{d\mathbf{v}_{sf,\alpha\beta}}{dt} \mathbf{i}_{s,\alpha\beta}^* \right) - \frac{3}{2} \text{Re} \left(\mathbf{v}_{sf,\alpha\beta} \frac{d\mathbf{i}_{s,\alpha\beta}^*}{dt} \right) \\ \frac{dQ_{sf}}{dt} = -\frac{3}{2} \text{Im} \left(\frac{d\mathbf{v}_{sf,\alpha\beta}}{dt} \mathbf{i}_{s,\alpha\beta}^* \right) - \frac{3}{2} \text{Im} \left(\mathbf{v}_{sf,\alpha\beta} \frac{d\mathbf{i}_{s,\alpha\beta}^*}{dt} \right) \end{cases}. \quad (44)$$

Note that the VM-DPC is designed based on an ideal grid voltage condition. Therefore, the differential of filtered grid voltage can be approximated as,

$$\frac{d}{dt} \mathbf{v}_{sf,\alpha\beta} \approx j\omega_s \mathbf{v}_{sf,\alpha\beta}. \quad (45)$$

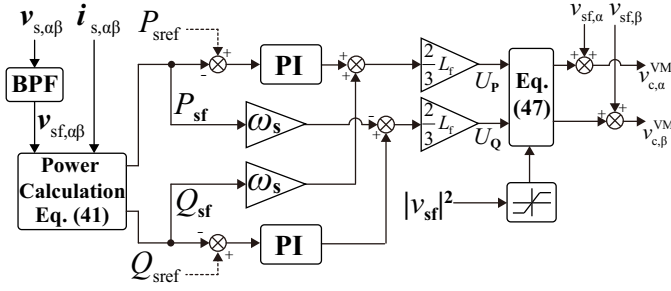


Fig. 7. Control scheme of voltage modulated direct power control (VM-DPC).

By substituting (2) and (45) into (44), the instantaneous variation of the active and reactive powers of VSC can be calculated as,

$$\begin{cases} \frac{dP_{sf}}{dt} = -\omega_s Q_{sf} - \frac{R_f}{L_f} P_{sf} + \frac{3}{2L_f} U_P \\ \frac{dQ_{sf}}{dt} = \omega_s P_{sf} - \frac{R_f}{L_f} Q_{sf} + \frac{3}{2L_f} U_Q \end{cases} \quad (46)$$

where U_P and U_Q are the power regulation inputs, which are,

$$\begin{cases} U_P = \text{Re}(\mathbf{v}_{sf,\alpha\beta} \mathbf{v}_{c,\alpha\beta}^*) - |\mathbf{v}_{sf}|^2 \\ U_Q = \text{Im}(\mathbf{v}_{sf,\alpha\beta} \mathbf{v}_{c,\alpha\beta}^*) \end{cases} \quad (47)$$

Based on (46) and (47), the power tracking can be designed in closed-loop using PI and power feedforward, which can be expressed as follows,

$$\begin{cases} U_P = \frac{2L_f}{3} G_{PI,dq}(s')(P_{sref} - P_{sf}) + \omega_s Q_{sf} \\ U_Q = \frac{2L_f}{3} G_{PI,dq}(s')(Q_{sref} - Q_{sf}) - \omega_s P_{sf} \end{cases} \quad (48)$$

Finally, the output VSC voltage can be decomposed into its fundamental and harmonic components as $\mathbf{v}_{c,\alpha\beta}^{VM} = \mathbf{v}_{c1,\alpha\beta}^{VM} + \mathbf{v}_{ch,\alpha\beta}^{VM}$, which can be deduced from (47) given as,

$$\begin{cases} \mathbf{v}_{c,\alpha}^{VM} = (\mathbf{v}_{sf,\alpha} U_P + \mathbf{v}_{sf,\beta} U_Q) / |\mathbf{v}_{sf}|^2 + \mathbf{v}_{sf,\alpha} \\ \mathbf{v}_{c,\beta}^{VM} = (\mathbf{v}_{sf,\beta} U_P - \mathbf{v}_{sf,\alpha} U_Q) / |\mathbf{v}_{sf}|^2 + \mathbf{v}_{sf,\beta} \end{cases} \quad (49)$$

Note that by substituting (43) and (48) into (46), the dynamics of the fundamental power tracking can be extracted and expressed in terms of the same equation given as (9),

$$\frac{\mathbf{S}_{s1}}{\mathbf{S}_{sref}} = \frac{K_p s' + K_i}{s'^2 + (K_p + \frac{R_f}{L_f})s' + K_i} \quad (50)$$

Therefore, it is found that VM-DPC and VOC share the same power tracking property. Moreover, VM-DPC has better tracking performance since it eliminates PLL [26]. The control scheme of VM-DPC is presented in Fig. 7.

It can be found from (49) that integration control of the powers inevitably result in a cross coupling between harmonic components and fundamental components. However, if the magnitude $\tilde{\mathbf{v}}_{shf}$ can be reduced by using the BPF, then, $\tilde{\mathbf{v}}_{ch,\alpha\beta}^{VM}$ can be approximately linearized [30]. The details of the linearization of $\tilde{\mathbf{v}}_{ch,\alpha\beta}^{VM}$ is presented as,

$$\tilde{\mathbf{v}}_{ch,\alpha\beta}^{VM} = G_{del}(s) G_{c,\alpha\beta}(s) \tilde{\mathbf{i}}_{sh,\alpha\beta} + G_{del}(s) G_{fil}(s) [1 + G_{VM}(s)] \tilde{\mathbf{v}}_{sh,\alpha\beta}, \quad (51)$$

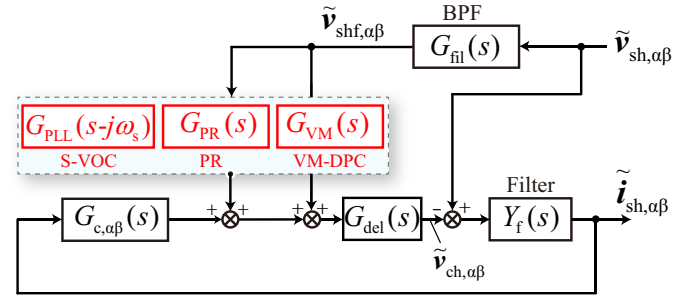


Fig. 8. Small-signal block diagram of grid-connected VSC using three symmetrical control strategies with BPF and voltage feedforward.

where $G_{c,\alpha\beta}(s)$ can be found equal to $G_{c,dq}(s')$ as follows,

$$G_{c,\alpha\beta}(s) = L_f (K_p + \frac{K_i}{s - j\omega_s} - j\omega_s) = G_{c,dq}(s'), \quad (52)$$

and $G_{VM}(s)$ can be written as,

$$G_{VM}(s) = \frac{2L_f K_p}{3|\mathbf{v}_{s1}^2|} (P_{sref} - jQ_{sref}). \quad (53)$$

The detailed admittance model of VSC using VM-DPC can be derived by substituting (51) into (4). The admittance model can be derived as,

$$\mathbf{Y}_{VSC}^{VM} = \frac{\tilde{\mathbf{i}}_{sh,\alpha\beta}}{\tilde{\mathbf{v}}_{sh,\alpha\beta}} = \mathbf{Y}_{VSC}^{PI} + \mathbf{Y}_n^{VM}. \quad (54)$$

where \mathbf{Y}_n^{VM} denotes the virtual admittance of VM-DPC, which represents the adverse effect of the VM-DPC on the basic admittance \mathbf{Y}_{VSC}^{PI} . The expression of \mathbf{Y}_n^{VM} is,

$$\mathbf{Y}_n^{VM} = - [1 + G_{del}(s) Y_f(s) G_{c,\alpha\beta}(s - j\omega_s)]^{-1} \cdot Y_f(s) G_{del}(s) G_{fil}(s) G_{VM}(s) \quad (55)$$

Finally, the small-signal block diagram of three symmetrical control strategies can be unified using the same frame as shown in Fig. 8. The differences of the block diagram of three methods are highlighted in red color. By comparing (53) with (40), it can be found the difference between $G_{PR}(s)$ and $G_{VM}(s)$ can be deduced as,

$$G_{PR}(s) - G_{VM}(s) = \frac{2L_f}{3|\mathbf{v}_{s1}^2|} \frac{2K_i}{s^2 + \omega_s^2} (P_{sref} - jQ_{sref}). \quad (56)$$

It shows that the difference between \mathbf{Y}_{VSC}^{PR} and \mathbf{Y}_{VSC}^{VM} gets Larger when the frequency of the harmonics is close to the fundamental frequency, i.e., $s = j\omega_h \approx j\omega_s$. On the other side, when ω_h is away from ω_s , it can be assumed that $\mathbf{Y}_{VSC}^{PR} \approx \mathbf{Y}_{VSC}^{VM}$ in the high- and low- frequency range.

IV. UNIFIED PERFORMANCE ANALYSIS

The unified dynamic response of three control strategies is discussed in this section. The power tracking dynamics of three

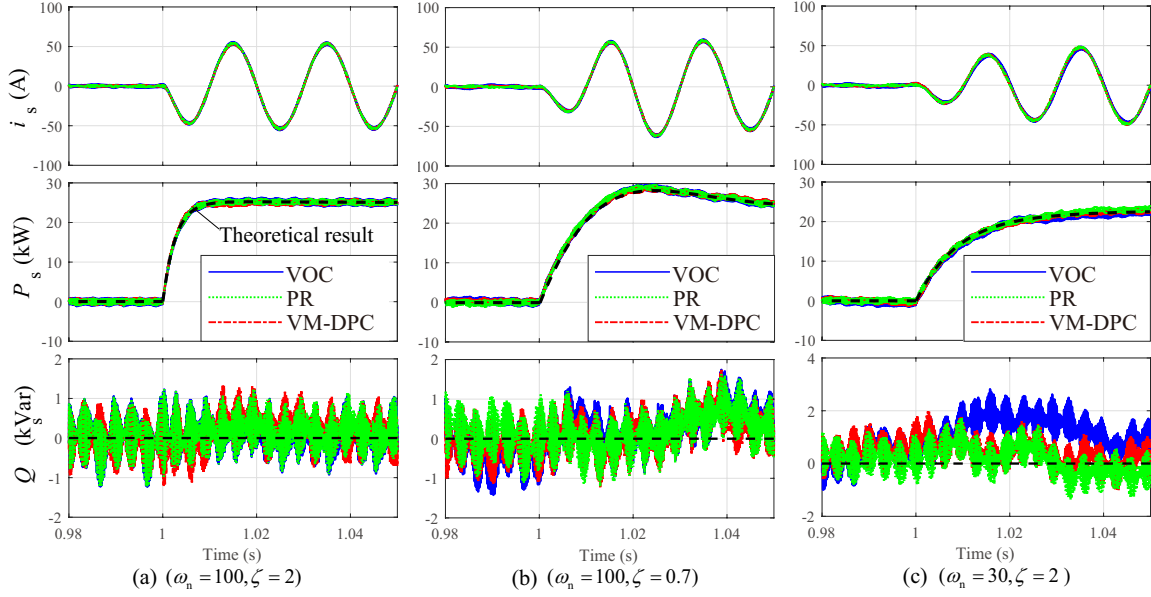


Fig. 9. Transient dynamics comparison of three different control methods under different control parameters. (a) $\omega_n = 100, \zeta = 2$. (b) $\omega_n = 100, \zeta = 0.7$. (c) $\omega_n = 30, \zeta = 2$

TABLE I
PARAMETERS OF SIMULATED GRID-CONNECTED VSC SYSTEM AND VM-DPC CONTROLLER

Parameter	Symbol	Value	Unit
Rated power	P_{sref}	25	kW
Switching frequency	f_w	4	kHz
Sampling frequency	f_{sa}	4	kHz
Time delay	T_{del}	0.0001	s
Fundamental frequency	f	50	Hz
Ground-to-line Voltage	$v_{s,rms}$	220	V
Natural frequency of BPF	ω_{fn}	314	rad/s
Damping ratio of BPF	ζ_f	0.1	
Dc voltage	v_{dc}	730	V
Filter resistance	R_f	0.12	Ω
Filter inductor	L_f	6	mH
Control Parameters			
Parameter	Value	Parameter	Value
K_p	121.4	K_i	10000
ω_n	100	ζ	0.7
$K_{PLL,p}$	1.5	$K_{PLL,i}$	130
f_{bw_PLL}	100 Hz		

frequency of 4 kHz. The dc-link voltage is set to 730 V. The VSC is connected to an ideal power grid. The circuit and control parameters are presented in Table I. Fig. 9 shows the simulation result of system step response with different control parameters. $\Delta P_{sref} = 25$ kW is set at 1s. Three different control settings are chosen, i.e., $(\omega_n = 100, \zeta = 2)$, $(\omega_n = 100, \zeta = 0.7)$, and $(\omega_n = 30, \zeta = 2)$. The black dotted line shows the dynamics response calculated based on (57). They are in agreement with the simulation results. It can be recognized that all three VSCs with different control methods track their references very well. Moreover, they also exhibit a similar transient response. The couplings between active and reactive power regulation of three methods are all small. It can be concluded that three different control methods have the same power tracking property. It can also be found that the system transient performance is improved either by increasing ω_n from 30 to 100 or increasing ζ from 0.7 to 2.

controllers can be deduced by transforming (9), (50) into the time domain as follows,

$$\begin{cases} S_s = S_{sref} \left\{ 1 + e^{-\zeta \omega_n t} \left[\left(\frac{K_p}{\omega_d} - \frac{\zeta}{\sqrt{1-\zeta^2}} \right) \sin(\omega_d t) - \cos(\omega_d t) \right] \right\}, \zeta < 1 \\ S_s = S_{sref} \left\{ 1 + e^{-\zeta \omega_n t} \left[\left(\frac{K_p}{\omega_d} - \frac{\zeta}{\sqrt{\zeta^2-1}} \right) \sinh(\omega_d t) - \cosh(\omega_d t) \right] \right\}, \zeta > 1 \end{cases} \quad (57)$$

where $\omega_d = \omega_n \sqrt{1-\zeta^2}$ denotes the natural damping frequency. To compare the transient response characteristics of different control strategies, a simulation is carried out in MATLAB/Simulink Simscape Power System. The IGBT switching signals are generated by using SVPWM with a switching

Note that the transient response in Fig. 9 are obtained under ideal grid conditions. The steady-state performance of VSC using different controllers is also tested under non-ideal grid conditions as presented in Fig. 10. The system performance under frequency variation conditions is shown in Fig. 10 (a). it can be observed that the PR control strategy leads to a steady-state error in the reactive power output. The system performance under three-phase voltage drop (0.2 p.u) and phase-A voltage drop (0.2 p.u) are tested, respectively as presented in Fig. 10 (b) and (c). It can be observed that three control strategies exhibit similar steady-state performance under the voltage drop conditions. In addition, note that the unbalanced voltage drop will cause power fluctuation and harmonic components. The reactive power fluctuation of VSC using the S-VOC is relatively large among the three control strategies, which is caused by the error of phase-locking under unbalanced grid conditions.

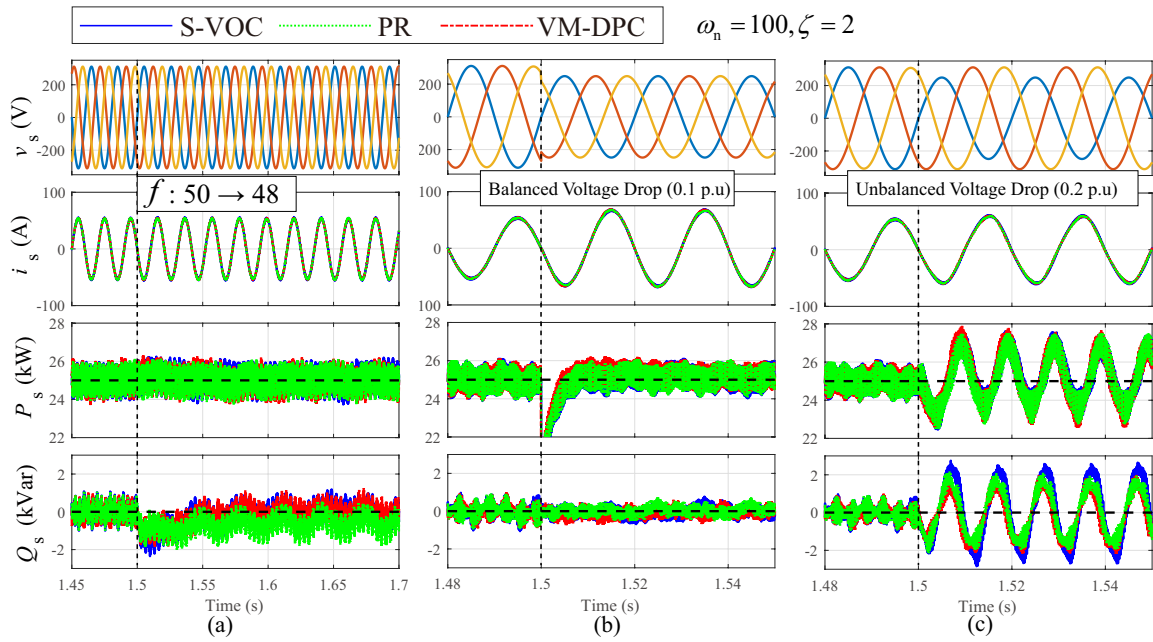


Fig. 10. Transient dynamics comparison of three different control methods under non-ideal grid conditions. (a) Frequency variation. (b) Balanced voltage drop condition. (c) Unbalanced voltage drop condition.

In this section, the unified transient performance of three control methods is analysed. Note that once the control parameters are determined, the basic admittance Y_{VSC}^{PI} is also determined. However, since each strategy has different additional admittance, their influence will affect the admittance characteristics and the grid-connection stability. In the next section, the admittance of three control methods is analysed, the accuracy of the admittance modeling is verified using the frequency-scan method. Moreover, the stability of the three control methods is compared based on the unified power tracking dynamics. In order to better explain the work of this paper, a diagram that summarizes the structure is presented in Fig. 11.

V. ADMITTANCE SPECIFICATION AND STABILITY ANALYSIS

This section determines the admittance specifications of the three control strategies. The circuit and control parameters are the same as presented in Table I.

A. Admittance Model Verification

The accuracy of the proposed admittance modeling can be verified through the frequency-scan method. The bode plots of the proposed admittance characteristic calculated based on (34), (54), and (41), are compared with the corresponding frequency-scan results as presented in Fig. 12. The frequency-scan results are carried out using detailed models which consider both the time delay and PWM. The control parameters of the comparison study is chosen as ($K_p = 121, K_i = 10000 \rightarrow \omega_n = 100, \zeta = 0.7$). The bandwidth of the symmetrical PLL is set to $f_{bw_PLL} = 100$ Hz. It can be observed that the harmonic response of grid-connected VSC using S-VOC

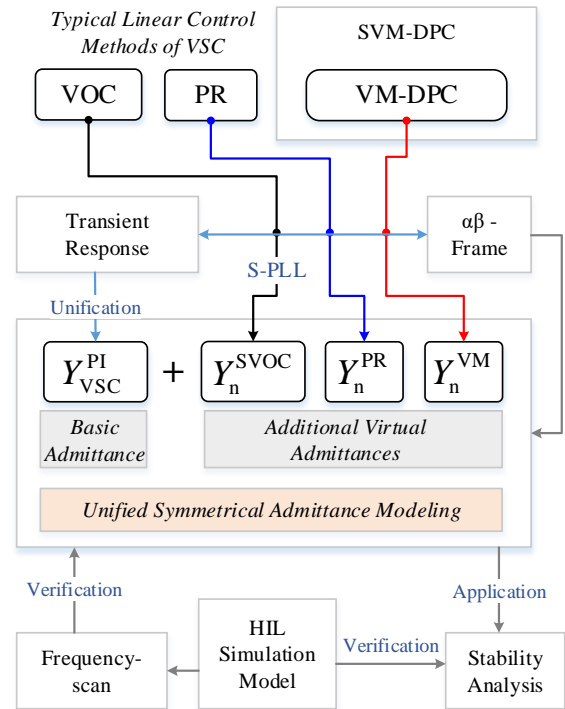


Fig. 11. Structure of the paper.

and PR are very close to each other. The difference of admittance characteristics is mainly reflected near the fundamental frequency (50 Hz), that the VSC using VM-DPC exhibits a comparatively low admittance magnitude, followed by the PR control and the S-VOC. Among the three control strategies, the S-VOC appears most sensitive to voltage harmonics, while

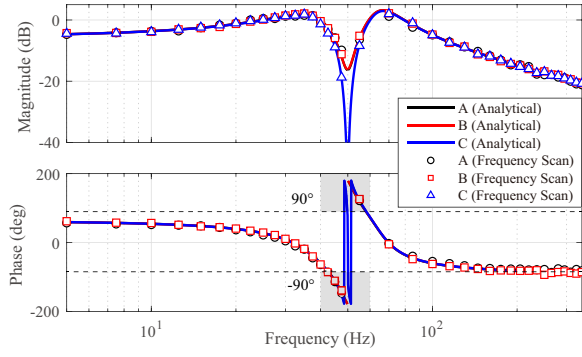


Fig. 12. Verification of the proposed admittance modelling with different control strategies ($\omega_n = 100$, $\zeta = 0.7$). (A) S-VOC, (B) PR control, (C) VM-DPC.

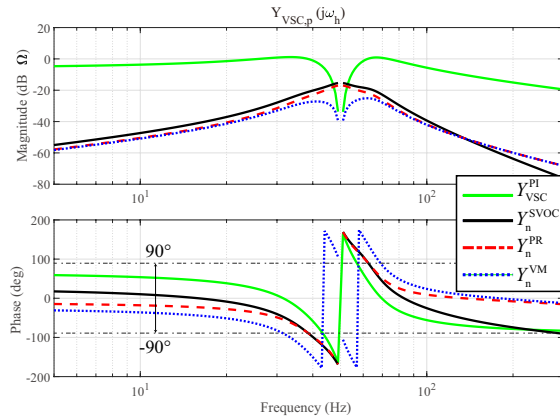


Fig. 13. Comparison between the basic admittance Y_{VSC}^{PI} and the virtual admittances of different symmetrical control methods.

VM-DPC seems to be the most robust one.

The adverse effect of the control structures on the equivalent admittance characteristics of grid-connected VSC is studied by comparing Y_{VSC}^{PI} to the virtual admittances Y_n^{SVOC} , Y_n^{VM} , and Y_n^{PR} , as presented in Fig. 13. It can be observed that in the high- and low- frequency range, the admittance characteristic of grid-connected VSC is mostly determined by the basic admittance Y_{VSC}^{PI} since $Y_{VSC}^{PI} \gg (Y_n^{SVOC}, Y_n^{VM}, Y_n^{PR})$. The virtual admittances Y_n^{VM} , Y_n^{SVOC} , and Y_n^{PR} successively show the negative damping characteristics, i.e., their phases are not within $-90^\circ \sim 90^\circ$, when the frequency moves close to 50 Hz. Since Y_n^{VM} exhibits the lowest magnitude, the negative damping of VM-DPC is the smallest among three strategies, which shows consistency with Fig. 12.

Fig. 14 shows a comparison of the analytical and frequency-scan results of the VSC equivalent admittances using different control strategies. The three different controllers are compared in separated figures. In each figure, the lines and dots with the same color denote the controllers that have the same control parameters. In other words, they share the same basic admittance Y_{VSC}^{PI} . Three groups of control parameters are selected, group (A) denotes ($K_p = 380$, $K_i = 10000 \rightarrow \omega_n = 100$, $\zeta = 2$), group (B) denotes ($K_p = 121$, $K_i = 10000$

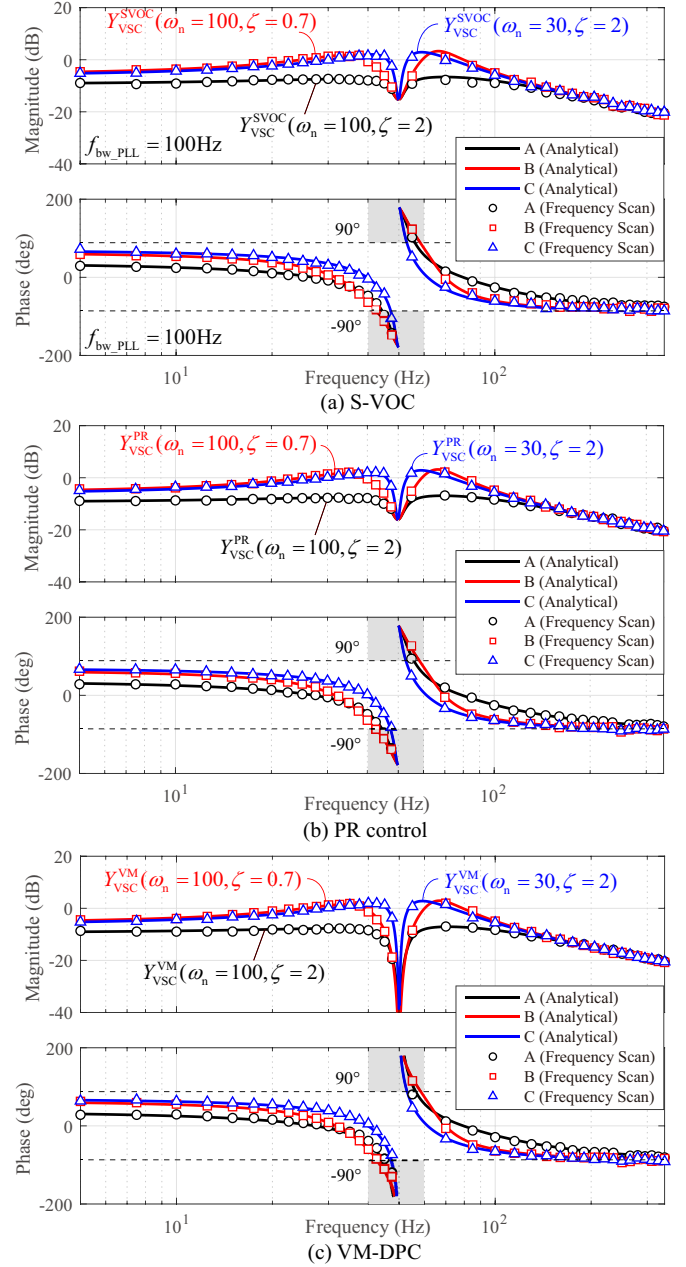


Fig. 14. Verification of the proposed admittance modelling under different control settings by using frequency-scan method. (a) Y_{VSC}^{SVOC} , (b) Y_{VSC}^{PR} , (c) Y_{VSC}^{VM} . (A) $\omega_n = 100$ rad/s, $\zeta = 0.7$, (B) $\omega_n = 100$ rad/s, $\zeta = 2$, (C) $\omega_n = 20$ rad/s, $\zeta = 0.7$.

$\rightarrow \omega_n = 100$, $\zeta = 0.7$), and group (C) denotes ($K_p = 100$, $K_i = 900 \rightarrow \omega_n = 30$, $\zeta = 2$), respectively. Moreover, when the parameters of the main controller change, the Bode plots of Y_{VSC}^{SVOC} , Y_{VSC}^{VM} , and Y_{VSC}^{PR} show similar variation rules. The results indicate that the decrease of damping ratio ζ and natural frequency ω_n will increase the magnitude of the system admittances, i.e., the system tends to be more sensitive to the voltage harmonics and becomes less stable under weak-grid connected conditions.

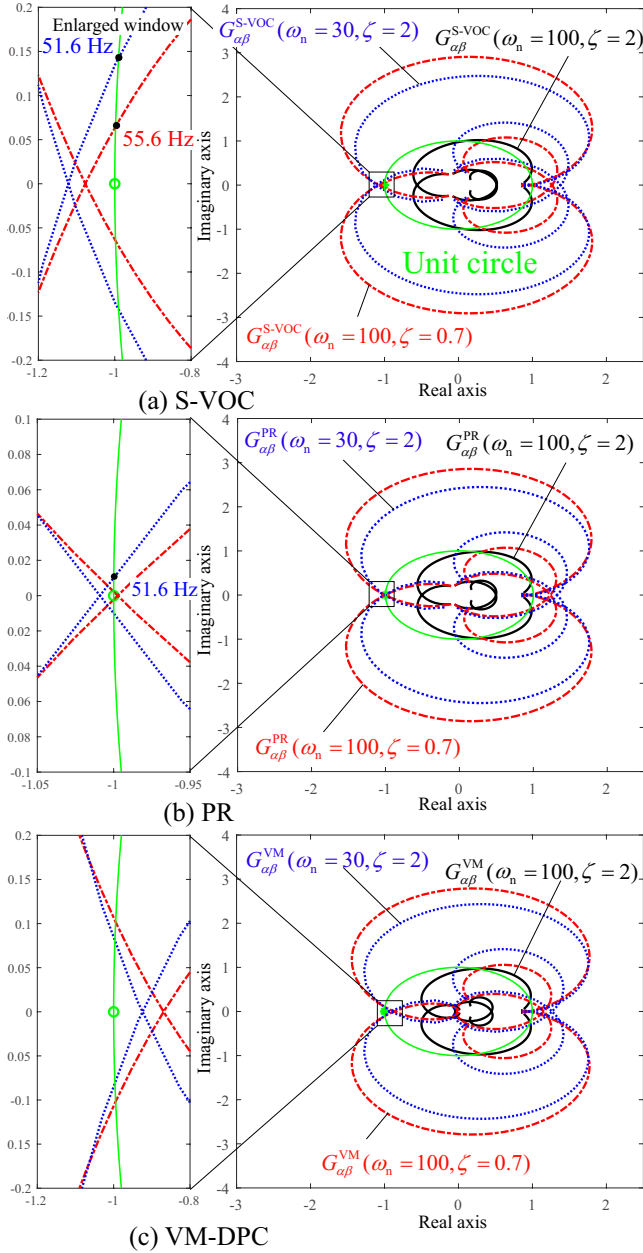


Fig. 15. Comparison of the Nyquist plots of three control methods with different control parameters.

B. Stability Analysis

In this subsection, the availability of the proposed method is verified by using the Nyquist stability criterion and simulation results. The grid admittance can be assumed as a simple, balanced R-L circuit, which can be expressed under the $\alpha\beta$ reference frame by using Laplace-transform as follows,

$$Y_{\text{grid}}(s) = \frac{1}{L_n s + R_n}, \quad (58)$$

where R_n is the grid resistance, L_n is the grid series inductance. The stability of the grid-connected VSC can be identified by using simple SISO Nyquist stability criterion [4]. The system can be simplified as Thevenin equivalent circuit consisting of the equivalent VSC admittance represented by

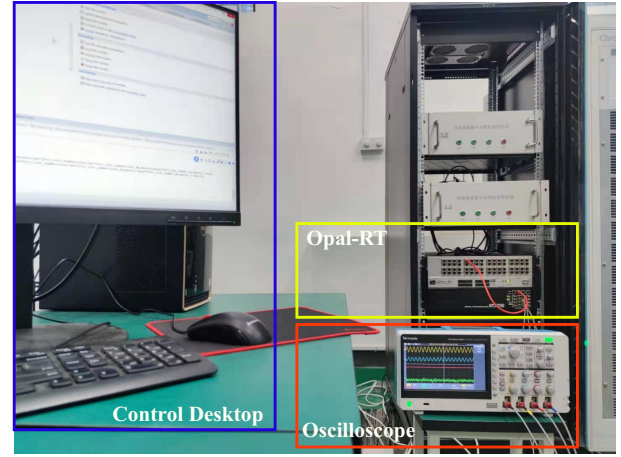


Fig. 16. Real-time simulation platform RTLAB from OPAL-RT for testing the three control methods.

Y_{VSC} , which are derived in (34), (54), and (41), respectively, and the grid admittance Y_{grid} . The stability of the system can be identified by the eigenvalues of the transfer function given as,

$$H_s = \frac{1}{1 + G_{\alpha\beta}(s)}, \quad (59)$$

where $G_{\alpha\beta}(s) = Y_{\text{VSC}}(s)/Y_{\text{grid}}(s)$ is the feedback characteristic equation of the system. Based on the linear-control theory that the closed-loop transfer function H_s guarantees stable operation only if $G_{\alpha\beta}(s)$ satisfies the Nyquist stability criterion, i.e., the encirclement of $(-1, j0)$ by the admittance ratio $G_{\alpha\beta}(s)$ is zero.

Fig. 15 shows a comparison of the Nyquist plot of $G_{\alpha\beta}(s)$ using different control methods. The VSCs are considered to be connected with grid with equivalent impedance ($L_n = 4.5$ mH, $R_n = 0.6 \Omega$). Three different control parameter settings are chosen as the same as in Fig. 14. The bandwidth of the symmetrical PLL is set to 100 Hz. Fig. 15 (a) shows the Nyquist diagram of $G_{\alpha\beta}(s)$ describing a grid-connected VSC using S-VOC. It can be seen that the encirclement around $(-1, 0)$ of the Nyquist curve $Y_{\text{VSC}}^{\text{S-VOC}}(s)/Y_{\text{grid}}(s)$ is zero when $\omega_n = 100, \zeta = 2$. However, the system becomes unstable when ζ changes from 2 to 0.7 and ω_n keeps 100 since the Nyquist curve encircles $(-1 + j0)$. It can be also found that the Nyquist curve intersects unit circle at 55.6 Hz, which also indicates the frequency of the oscillation component. A similar trend can be found when ω_n changes from 100 to 30 while $\zeta = 0.7$, the Nyquist curve encircles $(-1 + j0)$ and intersects unit circle at 51.9 Hz. From the enlarged window of Fig. 15 (b), it can be found that the point of intersection indicating $\omega_n = 100, \zeta = 0.7$, and $\omega_n = 30, \zeta = 2$, are very close to the critical point. Therefore, the system will be unstable. $G_{\alpha\beta}^{\text{PR}}$ with $\omega_n = 30$ and $\zeta = 2$ intersects the unit circle at 51.9 Hz. From Fig. 15 (c), it can be found all three curves avoid the critical point. Therefore, it can be concluded that the grid-connected VSC using the VM-DPC can maintain stable with all three control parameter settings.

The effectiveness of the Nyquist stability criterion based on proposed admittance modeling method is verified using

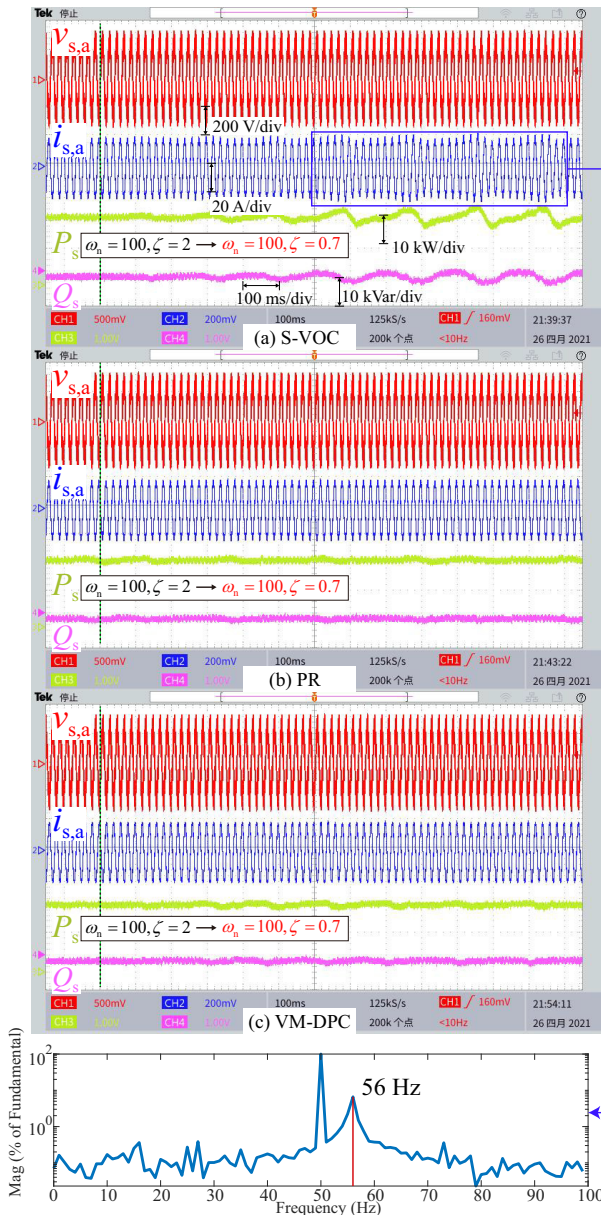


Fig. 17. Comparison of the grid interconnection test of the systems using different control methods when $(\omega_n = 100, \zeta = 0.7)$. (a) VOC with symmetrical PLL ($f_{bw_PLL} = 100$). (b) PR. (c) VM-DPC.

detailed simulation models implemented in real-time simulation platform RTLAB from Opal-RT as shown in Fig. 16. The circuit and the control parameters of the test are set as presented in Table I. Both time delay and PWM are considered in the simulation model. The VSCs are initially connected to a grid with equivalent impedance set as an inductor $L_n = 4.5$ mH in series with a resistance $R_n = 0.6 \Omega$. In Fig. 17, the control parameters are set to $(\omega_n = 100, \zeta = 2)$ at the beginning of the simulation. Then, the control parameters of three systems change to $(\omega_n = 100, \zeta = 0.7)$. The results indicate that the grid-connected VSC using S-VOC becomes unstable. The frequency of the main oscillation component is 56 Hz, which is consistent with the Nyquist stability analysis. On the other side, the VSC using the VM-DPC and PR still maintain stability after the change. Fig. 18 demonstrates the cases of

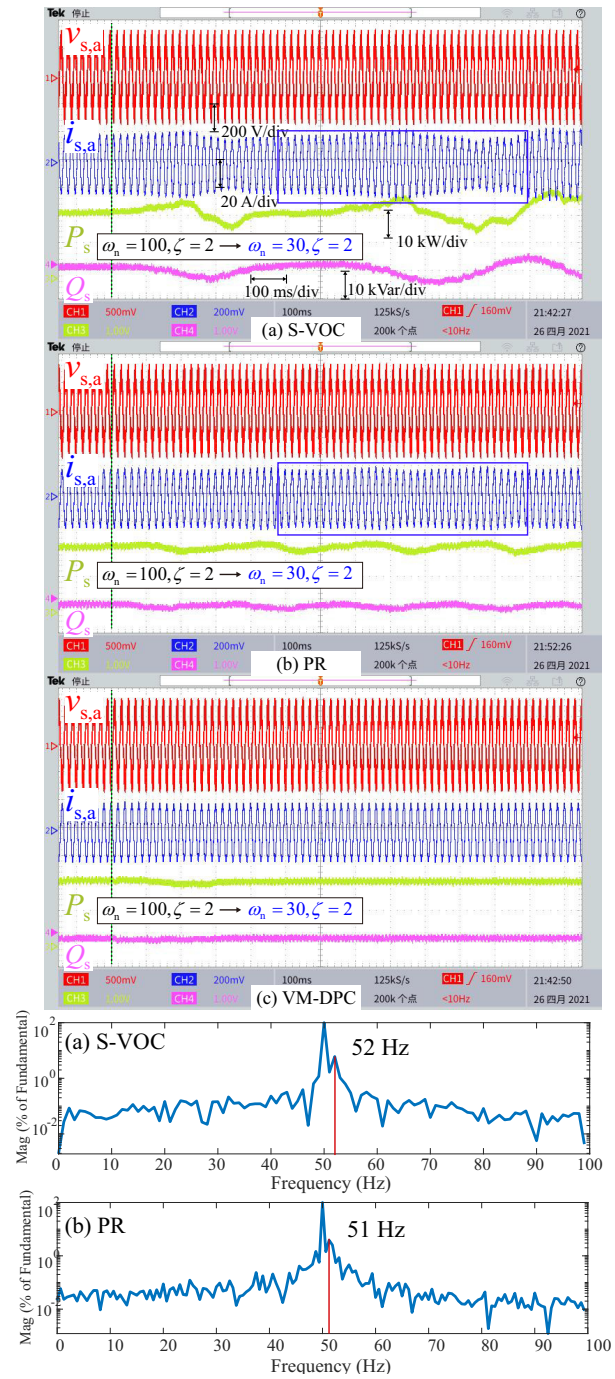


Fig. 18. Comparison of the grid interconnection test of the systems using different control methods under $(\omega_n = 30, \zeta = 2)$. (a) VOC with symmetrical PLL ($f_{bw_PLL} = 100$). (b) PR. (c) VM-DPC.

changing the control parameters from $(\omega_n = 100, \zeta = 2)$ to $(\omega_n = 30, \zeta = 2)$. It can be observed that VSCs using S-VOC and PR become out of control, and the powers start to oscillate after the parameters changing. The frequencies of the main oscillation components of the S-VOC and PR control are about 56 Hz and 51 Hz, which are consistent with the analytical results as presented in Fig. 15. The VSC using the VM-DPC control remains stable. Therefore, the accuracy of the admittance model and correctness of the Nyquist stability criterion are confirmed.

TABLE II
PROS AND CONS OF THE THREE CONTROL STRATEGIES

Control	Advantages	Disadvantages
VOC	<ul style="list-style-type: none"> • Robust to parameter/ frequency variations • Measurement of grid frequency 	<ul style="list-style-type: none"> • Use of coordinate transformation (dq frame) • Complex control structure
(PLL) (S-PLL)	<ul style="list-style-type: none"> • No frequency coupling 	<ul style="list-style-type: none"> • Frequency-coupling • Use of voltage magnitude
PR	<ul style="list-style-type: none"> • Simple structure 	<ul style="list-style-type: none"> • Affected by frequency variation
VM-DPC	<ul style="list-style-type: none"> • Robust to parameter/ frequency variations • Strong grid-connection stability • No coordinate transformation • Simple structure 	<ul style="list-style-type: none"> • PI control brings frequency-coupling

Finally, the pros and cons of VOC, PR and VM-DPC are summarized as presented in Table. II. The results prove that the VM-DPC exhibits satisfactory control performance at the same level as VOC and PR and shows the best grid-connection stability among the three control methods.

C. Experimental Verification

The transient response characteristics of the three control strategies at the same current loop bandwidth are also tested by using an experimental prototype as presented in Fig. 19. A three-phase 7.5 kW Danfoss converter with L-filter is connected to the grid. A grid simulator is used to generate 220 V rms voltage. A constant dc voltage is supplied using a dc power supply. The PCC line-to-line voltages and the currents are measured by using a DS2004 A/D board. The three different control strategies are implemented by using the dSPACE DS1007 system. The parameters of the system and controllers are chosen to be the same as presented in Table. I. The inner-loop control parameters are set to ($\omega_n = 408$, $\zeta = 2.47$). Fig. 20 shows the transient response of the three different methods when the reference of active power steps from 0 to 3 kW. Notice that three controllers have the same power convergence time of about 1.5 ms. The results confirm previous analysis that three different control methods have the same transient dynamic characteristics.

VI. CONCLUSION

In this paper, a uniformed comparative admittance analysis of grid-connected inverters using three symmetrical control strategies, i.e., S-VOC, PR control, and VM-DPC, is presented. The control methods are uniformed by the same power tracking dynamic expressed by a second-order transfer function. The admittance models of the three control methods considering voltage filtering and feedforward linearization are derived based on an unified framework, and the adverse effect of the different symmetrical controllers on the system harmonic response is compared by using virtual admittance. The simulation and experimental results show the transient response of three methods are the same. The experiment The

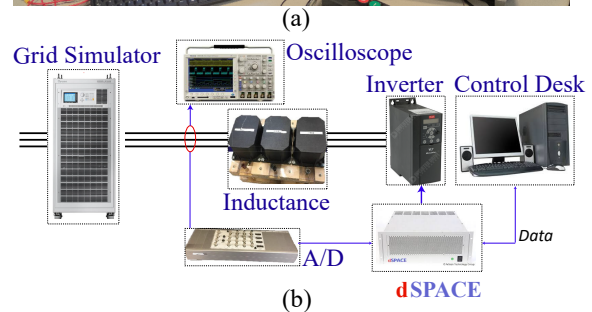
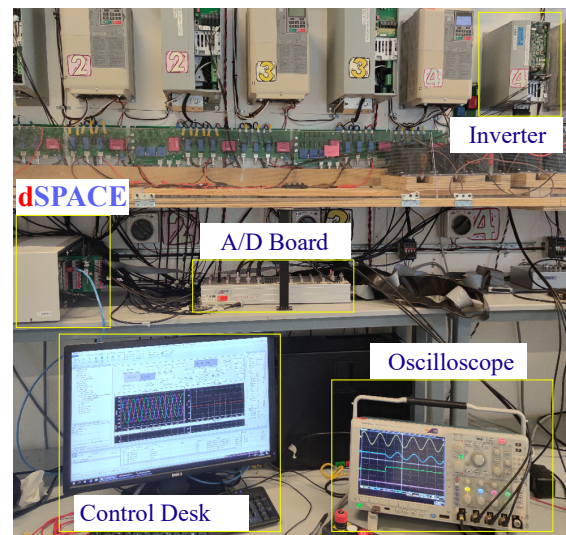


Fig. 19. Experimental setup at Aalborg University.

admittance analysis presents the difference in the admittance characteristics mainly reflect near the fundamental frequency. The grid-connected VSC using VM-DPC seems to be the least sensitive toward voltage harmonics. Moreover, it also exhibits the highest stability among the three symmetrical controllers. The bode plots of the equivalent admittances of the VSC using S-VOC and PR are very close to each other. The Nyquist stability criterion based on the proposed admittance modeling is verified by using the RTLAB simulation platform from Opal-RT.

ACKNOWLEDGEMENT

The authors would like to thank Dr. Chao Wu of Aalborg University, Aalborg, Denmark, for the experimental tests.

REFERENCES

- [1] F. Blaabjerg, Y. Yang, D. Yang, and X. Wang, "Distributed power-generation systems and protection," *Proc. IEEE*, vol. 105, no. 7, pp. 1311–1331, 2017.
- [2] L. Harnefors, "Modeling of three-phase dynamic systems using complex transfer functions and transfer matrices," *IEEE Trans. Ind. Electron.*, vol. 54, no. 4, pp. 2239–2248, 2007.
- [3] L. Harnefors, M. Bongiorno, and S. Lundberg, "Input-admittance calculation and shaping for controlled voltage-source converters," *IEEE Trans. Ind. Electron.*, vol. 54, no. 6, pp. 3323–3334, 2007.
- [4] J. Sun, "Impedance-based stability criterion for grid-connected inverters," *IEEE Trans. Power Electron.*, vol. 26, no. 11, pp. 3075–3078, 2011.
- [5] M. Cespedes and J. Sun, "Impedance modeling and analysis of grid-connected voltage-source converters," *IEEE Trans. Power Electron.*, vol. 29, no. 3, pp. 1254–1261, 2014.

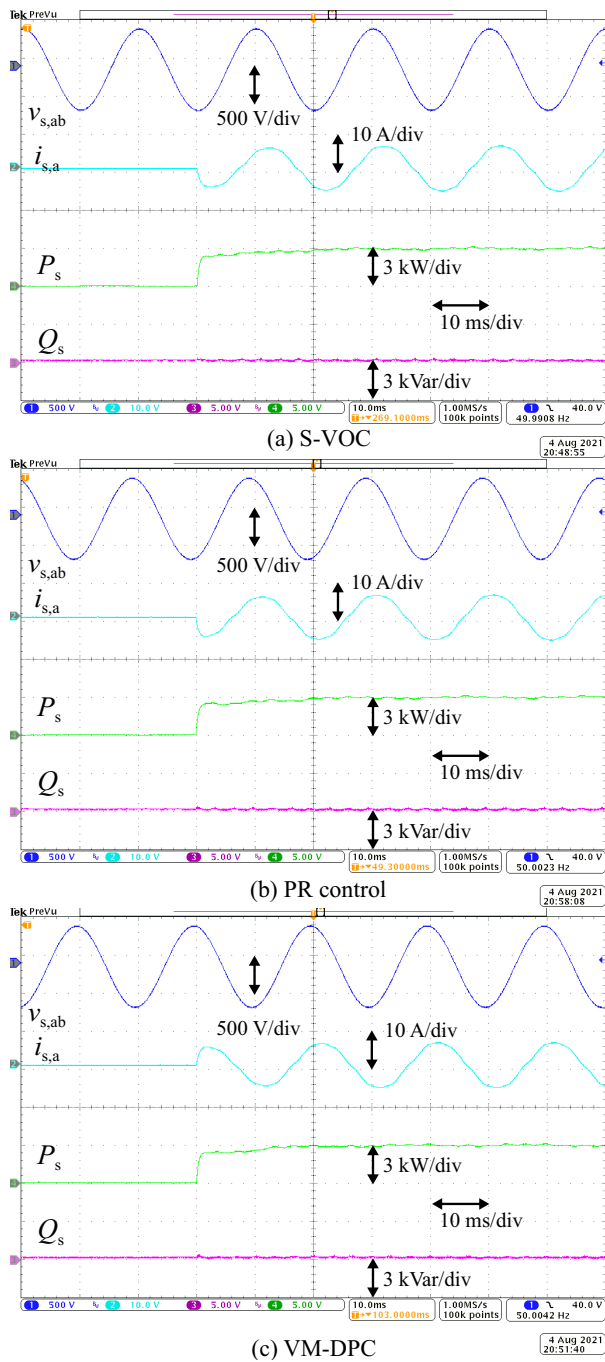


Fig. 20. Transient dynamics comparison of three different control methods. (a) S-VOC. (b) PR. (c) VM-DPC.

[6] B. Wen, D. Boroyevich, R. Burgos, P. Mattavelli, and Z. Shen, "Analysis of D-Q small-signal impedance of grid-tied inverters," *IEEE Trans. Power Electron.*, vol. 31, no. 1, pp. 675–687, 2016.

[7] X. Wang, L. Harnfors, and F. Blaabjerg, "Unified impedance model of grid-connected voltage-source converters," *IEEE Trans. Power Electron.*, vol. 33, no. 2, pp. 1775–1787, 2018.

[8] D. Yang, X. Wang, F. Liu, K. Xin, Y. Liu, and F. Blaabjerg, "Symmetrical PLL for SISO impedance modeling and enhanced stability in weak grids," *IEEE Trans. Power Electron.*, vol. 35, no. 2, pp. 1473–1483, 2019.

[9] Erdiwansyah, Mahidin, H. Husin, Nasaruddin, M. Zaki, and Muhibuddin, "A critical review of the integration of renewable energy sources with various technologies," *Prot. Control Mod. Power Syst.*, vol. 6, no. 1, 2021.

[10] Q. Liu, T. Caldognetto, and S. Buso, "Review and Comparison of Grid-Tied Inverter Controllers in Microgrids," *IEEE Trans. Power Electron.*, vol. 35, no. 7, pp. 7624–7639, 2020.

[11] M. Amin and M. Molinas, "Understanding the origin of oscillatory phenomena observed between wind farms and HVdc systems," *IEEE J. Emerg. Sel. Top. Power Electron.*, vol. 5, no. 1, pp. 378–392, 2017.

[12] A. Rygg, M. Molinas, Z. Chen, and X. Cai, "A modified sequence domain impedance definition and its equivalence to the dq-domain impedance definition for the stability analysis of AC power electronic systems," *IEEE J. Emerg. Sel. Top. Power Electron.*, vol. 4, no. 4, pp. 1383–1396, 2016.

[13] Y. Zhang, J. Liu, H. Yang, and J. Gao, "Direct power control of pulswidth modulated rectifiers without DC voltage oscillations under unbalanced grid conditions," *IEEE Trans. Ind. Electron.*, vol. 65, no. 10, pp. 7900–7910, 2018.

[14] Z. Miao, "Impedance-model-based SSR analysis for type 3 wind generator and series-compensated network," *IEEE Trans. Energy Convers.*, vol. 27, no. 4, pp. 984–991, 2012.

[15] K. Sun, W. Yao, J. Fang, X. Ai, J. Wen, and S. Cheng, "Impedance Modeling and Stability Analysis of Grid-Connected DFIG-based Wind Farm with a VSC-HVDC," *IEEE Journal of Emerging and Selected Topics in Power Electronics*, vol. 8, no. 2, pp. 1375–1390, 2019.

[16] H. Nian, B. Hu, Y. Xu, C. Wu, L. Chen, and F. Blaabjerg, "Analysis and reshaping on impedance characteristic of DFIG system based on symmetrical PLL," *IEEE Trans. Power Electron.*, vol. 35, no. 11, pp. 11720–11730, 2020.

[17] S. Fukuda and T. Yoda, "A novel current-tracking method for active filters based on a sinusoidal internal model," *IEEE Trans. Ind. Appl.*, vol. 37, no. 3, pp. 888–895, 2001.

[18] S. Li, X. Wang, Z. Yao, T. Li, and Z. Peng, "Circulating current suppressing strategy for MMC-HVDC based on nonideal proportional resonant controllers under unbalanced grid conditions," *IEEE Trans. Power Electron.*, vol. 30, no. 1, pp. 387–397, 2015.

[19] R. A. Fantino, C. A. Busada, and J. A. Solsona, "Optimum PR Control Applied to LCL Filters with Low Resonance Frequency," *IEEE Trans. Power Electron.*, vol. 33, no. 1, pp. 793–801, 2018.

[20] Y. Liao and X. Wang, "Stationary-frame complex-valued frequency-domain modeling of three-phase power converters," *IEEE J. Emerg. Sel. Top. Power Electron.*, vol. 8, no. 2, pp. 1922–1933, 2019.

[21] B. Xie, K. Guo, M. Mao, L. Zhou, T. Liu, Q. Zhang, and G. Hao, "Analysis and Improved Design of Phase Compensated Proportional Resonant Controllers for Grid-Connected Inverters in Weak Grid," *IEEE Trans. Energy Convers.*, vol. 35, no. 3, pp. 1453–1464, 2020.

[22] L. Harnfors, S. Member, X. Wang, A. G. Yepes, and F. Blaabjerg, "Passivity-based stability assessment of grid-connected VSCs—an overview," *IEEE J. Emerg. Sel. Topics Power Electron.*, vol. 4, no. 1, pp. 116–125, 2016.

[23] P. Antoniewicz and M. P. Kazmierkowski, "Virtual-flux-based predictive direct power control of AC/DC converters with online inductance estimation," *IEEE Trans. Ind. Electron.*, vol. 55, no. 12, pp. 4381–4390, 2008.

[24] J. Hu, L. Shang, Y. He, and Z. Q. Zhu, "Direct active and reactive power regulation of grid-connected DC/AC converters using sliding mode control approach," *IEEE Trans. Power Electron.*, vol. 26, no. 1, pp. 210–222, 2011.

[25] Y. Gui, X. Wang, F. Blaabjerg, and D. Pan, "Control of Grid-Connected Voltage-Source Converters: The Relationship between Direct-Power Control and Vector-Current Control," *IEEE Ind. Electron. Mag.*, vol. 13, no. 2, pp. 31–40, 2019.

[26] Y. Gui, F. Blaabjerg, X. Wang, J. Bendtsen, D. Yang, and J. Stoustrup, "Improved DC-link voltage regulation strategy for grid-connected converters," *IEEE Trans. Ind. Electron.*, 2020 in press.

[27] S. Mensou, A. Essadki, T. Nasser, and B. Bououlid Idrissi, "A direct power control of a DFIG based-WECS during symmetrical voltage dips," *Prot. Control Mod. Power Syst.*, vol. 5, no. 1, 2020.

[28] S. Gao, H. Zhao, Y. Gui, D. Zhou, and F. Blaabjerg, "An Improved Direct Power Control for Doubly Fed Induction Generator," *IEEE Trans. Power Electron.*, vol. 36, no. 4, pp. 4672–4685, 2021.

[29] S. Gao, H. Zhao, Y. Gui, D. Zhou, V. Terzija, and F. Blaabjerg, "A novel direct power control for DFIG with parallel compensator under unbalanced grid condition," *IEEE Trans. Ind. Electron.*, 2020 in press.

[30] S. Gao, H. Zhao, Y. Gui, J. Luo, and F. Blaabjerg, "Impedance Analysis of Voltage Source Converter Using Direct Power Control," *IEEE Trans. Energy Convers.*, 2020 in press.

[31] Y. Gui, M. Li, J. Lu, S. Golestan, J. M. Guerrero, and J. C. Vasquez, "A voltage modulated DPC approach for three-phase PWM rectifier," *IEEE Trans. Ind. Electron.*, vol. 65, no. 10, pp. 7612–7619, 2018.



Shuning Gao (S'17) received the B.S. degree in electrical engineering from Huazhong University of Science and Technology, Wuhan, China, in 2015. He is currently working toward the Ph.D. degree in the Shandong University.

In December 2019, he was a visiting student with the Automation & Control Section, Department of Electronic Systems, Aalborg University. His research interests include modeling and control of power electronics, stability analysis of power electronics based power systems.



Haoran Zhao (S'12-M'15-SM'17) received the B.E. degree from Shandong University, China, in 2005, the M.E. degree from the Technical University of Berlin, Germany, in 2009, and the Ph.D. degree from Technical University of Denmark, Denmark, in 2014. Currently, he is a professor with the School of Electrical Engineering, Shandong University, China.

He was an Electrical Engineer with State Grid Corporation of China (SGCC), in 2005. From 2010 to 2011, he worked as an Application Developer in DlgSILENT GmbH, Germany. His research interests

include modeling and integration study of wind power, control of energy storage system, and integrated energy systems.



Peng Wang received M.E. degree from Shandong University, China, in 2014, and the the Dr.-Ing. (summa cum laude) degree from Technical University of Berlin, Germany, in 2020. He is currently working in the School of Electrical Engineering, Shandong University, China. He was an Electrical Engineer with State Grid Corporation of China (SGCC), in 2018. His current research interests include modeling and stability analysis of AC-DC power system integrated with renewable generation.



Yonghao Gui (S'11-M'17-SM'20) received the B.S. degree in automation from Northeastern University, Shenyang, China, in 2009, and the M.S. and Ph.D. degrees in electrical engineering from Hanyang University, Seoul, South Korea, in 2012 and 2017, respectively.

From Feb. 2017 to Nov. 2018, he worked with the Department of Energy Technology, Aalborg University, Aalborg, Denmark, as a Postdoctoral Researcher. Since Dec. 2018, he has been working with the Automation & Control Section, Department of Electronic Systems, Aalborg University, Aalborg, Denmark, where he is currently an Assistant Professor. His research interests include Control of Power Electronics in Power Systems, Energy Internet, and Smart Grids.

Dr. Gui has served as an Associate Editor for the IEEE Transaction on Energy Conversion, IEEE Power Engineering Letter, IEEE Access, and International Journal of Control, Automation and Systems (IJCAS). He was a recipient of the IEEE Power & Energy Society General Meeting Best Conference Paper Award in 2019 and the IJCAS Academic Activity Award 2019.



Vladimir Terzija (M'95-SM'00-F'16) was born in Donji Baraci (former Yugoslavia). He received the Dipl.-Ing., M.Sc., and Ph.D. degrees in electrical engineering from the University of Belgrade, Belgrade, Serbia, in 1988, 1993, and 1997, respectively.

He is the Engineering and Physical Science Research Council (EPSRC) Chair Professor in Power System Engineering with the School of Electrical and Electronic Engineering, The University of Manchester, Manchester, U.K., where he has been since 2006. From 1997 to 1999, he was an Assistant

Professor at the University of Belgrade, Belgrade, Serbia. From 2000 to 2006, he was a senior specialist for switchgear and distribution automation with ABB, Ratingen, Germany. His current research interests include smart grid applications; wide-area monitoring, protection, and control; multi-energy systems; switchgear and transient processes; ICT, data analytics and digital signal processing applications in power systems.

Prof. Terzija is Editor in Chief of the International Journal of Electrical Power and Energy Systems, Alexander von Humboldt Fellow, as well as a DAAD and Taishan Scholar. He is the recipient of the National Friendship Award, China (2019). Since 2018, he is the National Thousand Talents Distinguished Professor at Shandong University, China.



Frede Blaabjerg (S'86-M'88-SM'97-F'03) was with ABB-Scandia, Randers, Denmark, from 1987 to 1988. From 1988 to 1992, he got the PhD degree in Electrical Engineering at Aalborg University in 1995. He became an Assistant Professor in 1992, an Associate Professor in 1996, and a Full Professor of power electronics and drives in 1998. From 2017 he became a Villum Investigator. He is honoris causa at University Politehnica Timisoara (UPT), Romania and Tallinn Technical University (TTU) in Estonia.

His current research interests include power electronics and its applications such as in wind turbines, PV systems, reliability, harmonics and adjustable speed drives. He has published more than 600 journal papers in the fields of power electronics and its applications. He is the co-author of four monographs and editor of ten books in power electronics and its applications.

He has received 33 IEEE Prize Paper Awards, the IEEE PELS Distinguished Service Award in 2009, the EPE-PEMC Council Award in 2010, the IEEE William E. Newell Power Electronics Award 2014, the Villum Kann Rasmussen Research Award 2014, the Global Energy Prize in 2019 and the 2020 IEEE Edison Medal. He was the Editor-in-Chief of the IEEE TRANSACTIONS ON POWER ELECTRONICS from 2006 to 2012. He has been Distinguished Lecturer for the IEEE Power Electronics Society from 2005 to 2007 and for the IEEE Industry Applications Society from 2010 to 2011 as well as 2017 to 2018. In 2019-2020 he served as a President of IEEE Power Electronics Society. He has been Vice-President of the Danish Academy of Technical Sciences. He is nominated in 2014-2020 by Thomson Reuters to be between the most 250 cited researchers in Engineering in the world.